https://doi.org/10.5194/egusphere-2026-569
Preprint. Discussion started: 20 February 2026
© Author(s) 2026. CC BY 4.0 License.

High climatological cloud cover limits its response to aerosols in ICON-HAM

Yichen Jia [1, 2], Hendrik Andersen [1, 2], David Neubauer [3, *], Ulrike Lohmann [3], Corinna Hoose [4], and Jan Cermak [1, 2]

[1]Institute of Meteorology and Climate Research Atmospheric Trace Gases and Remote Sensing (IMKASF), Karlsruhe Institute of Technology (KIT), Karlsruhe, Germany
[2]Institute of Photogrammetry and Remote Sensing, Karlsruhe Institute of Technology (KIT), Karlsruhe, Germany
[3]Institute for Atmospheric and Climate Science, ETH Zurich, Zurich, Switzerland
[4]Institute of Meteorology and Climate Research Troposphere Research (IMKTRO), Karlsruhe Institute of Technology (KIT), Karlsruhe, Germany
[*]now at: GeoSphere Austria, Vienna, Austria

Correspondence: Yichen Jia (yichen.jia@kit.edu)

Abstract.

Marine low-level clouds substantially cool the climate and are sensitive to aerosols. Observations suggest strong cooling from cloud fraction (CF) adjustments, yet global climate models (GCMs) may underestimate this process. We apply explainable machine-learning with SHapley Additive exPlanations (SHAP) to the ICOsahedral Nonhydrostatic atmosphere model coupled with the Hamburg Aerosol Module (ICON-HAM) to quantify CF sensitivity to cloud droplet number concentration (N_d). We analyze six experiments combining two cloud cover parameterizations, an RH-only scheme (CC–RH) and a cloud-water-dependent scheme (CC–RH–LWC), with three prescribed lower bounds for N_d ($N_\mathrm{d,min}$ = 10, 40, 100 cm^{-3}). The $\ln N_\mathrm{d}$–CF relationships in ICON–HAM are more nonlinear than in satellite observations and exhibit saturation. We quantify sensitivities using piecewise linear regression (PLR) separating low- and high-N_d regimes. Sensitivities are stronger in the low-N_d regime, while inter-scheme and inter-$N_\mathrm{d,min}$ differences are negligible at high N_d. Unexpectedly, CC-RH-LWC shows weaker sensitivity than CC-RH at high $N_\mathrm{d,min}$, despite explicit CF–cloud water coupling. We attribute this to a "headroom effect": higher $N_\mathrm{d,min}$ suppresses autoconversion and enhances liquid water path in both schemes, but CC-RH-LWC converts this into higher mean CF, limiting headroom for aerosol-induced CF increases. These findings are robust across three PLR breakpoint strategies. Our results demonstrate that GCM CF responses are state-dependent and strongly influenced by model configuration choices, which can pre-saturate cloud cover responses and true CF adjustment magnitudes. We suggest that model–observation comparisons should account for baseline mean CF to avoid misinterpretation.

https://doi.org/10.5194/egusphere-2026-569
Preprint. Discussion started: 20 February 2026
© Author(s) 2026. CC BY 4.0 License.

1 Introduction

More than 23 % of the Earth's ocean surface is covered by marine low-level clouds (MLCs) (Wood, 2012). Due to the small temperature difference between MLC tops and the ocean surface, their impact on outgoing longwave radiation is limited. However, MLCs greatly reflect incoming shortwave radiation and thus exert a strong net cooling effect on the climate system (Hartmann et al., 1992). Because they are so widespread over the dark ocean surface, MLCs are extremely important for the Earth's radiative balance (Wood, 2012; Chen et al., 2014). Anthropogenic aerosols modify the radiative effect of MLCs by acting as cloud condensation nuclei (CCN), thus influencing the coverage and properties of clouds. Compared to continental clouds and other marine cloud types, MLCs tend to be particularly responsive to aerosol perturbations (Wood et al., 2015) owing to their large areal coverage, the prevalence of relatively optically thin clouds (optical depth <3) (Leahy et al., 2012), and their development in relatively clean regions with less anthropogenic aerosol influence (Platnick and Twomey, 1994).

Cloud droplet number concentration (N_d) increases with more atmospheric aerosols, leading to smaller cloud droplet effective radii, assuming a constant liquid water path (LWP), thus leads to brighter clouds and an instantaneous negative top-of-atmosphere (TOA) radiation change (Twomey effect, (Twomey, 1977)). Subsequently, the reduced collision and coalescence efficiency of the smaller-sized droplets delays precipitation and prolongs the lifetime of clouds, ultimately resulting in a greater cloud fraction (CF) and LWP (Albrecht, 1989). However, particularly in non-precipitating clouds, reducing droplet sizes can also reduce CF and LWP by enhancing cloud-top entrainment, either via shorter evaporation timescales (Wang et al., 2003; Small et al., 2009) or via decreased sedimentation, which can retain liquid water in the entrainment zone (Ackerman et al., 2004; Bretherton et al., 2007). These cloud processes that exert influence independent of surface air temperature changes are referred to as cloud adjustments (Boucher et al., 2013; Sherwood et al., 2015), including CF and LWP adjustments. The instantaneous effect of aerosols on the TOA radiation balance due to changes in N_d, and the subsequent CF and LWP adjustments together are known as effective radiative forcing from aerosol-cloud interactions (ACI), contributing to a large source of uncertainty in the quantification of climate change (Forster et al., 2021; Watson-Parris and Smith, 2022).

Over the past decade, systematic differences in the magnitude of cloud adjustments have been found between models and observations (Gryspeerdt et al., 2020; Quaas et al., 2024). In the most recent two eras of the Coupled Model Intercomparison Project (CMIP5 and CMIP6) in particular, GCMs consistently show strong cooling driven by the Twomey effect and LWP adjustments (Smith et al., 2020; Zelinka et al., 2023). By comparision, observational studies generally find a weak or ambiguous LWP response to aerosol perturbations (Malavelle et al., 2017; Bender et al., 2019; Toll et al., 2019).

For the CF adjustment, observational studies agree on the sign while disagree on the magnitude of the CF sensitivity to aerosol (proxies) or resulting negative forcing (Gryspeerdt et al., 2016; Andersen et al., 2017; Fuchs et al., 2018; Rosenfeld et al., 2019; Wall et al., 2022; Jia et al., 2024). GCMs agree with observational studies in terms of the positive relationship between cloud cover and aerosols and therefore a negative radiative forcing from the CF adjustment (Zelinka et al., 2014; Forster et al., 2021), as autoconversion parameterizations in many of these models allow aerosols and thus N_d to suppress precipitation and thereby prolong cloud lifetime (Bellouin et al., 2020). However, while models agree on the sign of the CF adjustment, they diverge on the magnitude and relative importance of the Twomey effect, the LWP adjustment and the CF adjustment.

GCMs simulate a minimal or negligible CF contribution relative to the Twomey effect and LWP adjustment (Smith et al., 2020; Zelinka et al., 2023). Even when diagnosed using a consistent cloud radiative kernel method, multiple CMIP6 models suggest a CF adjustment being weaker than both the Twomey effect and LWP adjustment (Duran et al., 2025), whereas the same framework applied to satellite observations indicates that the CF adjustment outweighs both (Wall et al., 2023). Consistent with this, a recent model–observation comparison (Wang et al., 2025) showed that multiple GCMs failed to reproduce the strong aerosol-induced increase in cloud cover associated with the Holuhraun volcanic eruption documented by Chen et al. (2022). Taken together, the discrepancies in the magnitudes and relative importance of LWP and CF adjustments suggest that LWP adjustments are likely overestimated and CF adjustments are underestimated in GCMs. In particular, recent observational evidence increasingly highlights the CF adjustment as potentially the largest contributor to effective radiative forcing due to ACI (e.g. Chen et al., 2022; Yuan et al., 2023; Wall et al., 2023; Chen et al., 2024), providing a key motivation for this present work. Moreover, the CF response to aerosols may saturate under already polluted conditions, further complicating its quantification. For example, Wang et al. (2024) found over high-latitude oceans that the CF responses saturate once N_d exceeds around 60 cm^{-3}, suggesting that background cloud conditions influence the CF adjustment.

The challenge comes from the fact that observational constraints on the CF adjustment often rely on opportunistic experiments, such as ship tracks and volcanic events, which can rule out confounding meteorological covariates. However, ship tracks are typically subscale for GCMs, while volcanic eruptions can be episodic and often involve uncertain emissions, making the quantification challenging. Therefore, both approaches may lack global representativeness. The alternative is to use large-scale satellite studies, which are spatiotemporally representative and good for constraining GCMs, but use different ways of dealing with meteorological confounders. For example, Gryspeerdt et al. (2016) has attempted to address this confounding issue through statistical control of confounding variables such as relative humidity (RH), or Andersen et al. (2023) has incorporated them into a machine-learning (ML) framework using ridge regression.

In a previous study (Jia et al., 2024, hereafter J24), we quantified the CF adjustment as the sensitivity of MLC CF to N_d using an explainable ML framework trained on Moderate Resolution Imaging Spectroradiometer (MODIS) observations and reanalysis data from the European Centre for Medium-Range Weather Forecasts. This eXtreme Gradient Boosting (XGBoost) and SHapley Additive exPlanation (SHAP) framework demonstrated global positive N_d–CF relationships.

In this study, we extend the explainable ML framework of J24 to Atmospheric Model Intercomparison Project (AMIP) simulations with the ICOsahedral Nonhydrostatic (ICON) atmosphere model coupled with the Hamburg Aerosol Module (HAM) (ICON-HAM). The main goals of this study are twofold: (1) to enable a consistent comparison between observation- and model-based N_d–CF sensitivities; (2) to investigate how structural model choices shape the simulated CF response. To achieve this, we conduct six simulations that combine two cloud-cover schemes (CC-RH, dependent only on RH, and CC-RH-LWC, additionally dependent on cloud water content) with three prescribed lower bounds for cloud droplet number concentration ($N_\mathrm{d,min}$ = 10, 40 and 100 cm^{-3}), examining their joint impact. As in J24, we quantify the sensitivity of MLC CF to log-transformed N_d ($\ln N_\mathrm{d}$) using regional XGBoost models with SHAP, extended via a piecewise linear regression (PLR) to accommodate the stronger nonlinear response in ICON-HAM. Guided by these goals, our hypotheses are: (1) the $\ln N_\mathrm{d}$–CF relationships diagnosed from ICON-HAM differ quantitatively, or maybe even qualitatively, from the MODIS-based relationships in J24; (2) given the stronger coupling between cloud water content and cloud cover in CC-RH-LWC, we expect this scheme to exhibit larger $\ln N_\mathrm{d}$–CF sensitivities than the RH-only scheme with prescribed $N_\mathrm{d,min}$ expected to further modulate these sensitivities differently in each scheme.

2 Data and Methods

2.1 ICON-HAM experimental setup

2.1.1 ICON-HAM general model description

The host model in this study is the ICON atmospheric model (Giorgetta et al., 2018), coupled with HAM to obtain a global atmosphere-aerosol model. The overall coupled model configuration largely follows that described in Salzmann et al. (2022), although we use a more recently developed ICON version 2.6.4 combined with the same HAM version 2.3 as in their study. Hereafter, without explicit notation, ICON-HAM refers to ICON2.6.4-HAM2.3. The ICON dynamical core provides a nonhydrostatic, compressible atmosphere on an icosahedral grid. HAM simulates aerosol properties such as size distributions and couples them to clouds and radiation, enabling process-level links between aerosol perturbations and cloud responses. In this study, the ICON-HAM model uses an R02B04 horizontal grid, corresponding to a grid spacing of approximately 160 km between neighbouring grid points, with 47 vertical levels using a hybrid sigma-height coordinate system. A code fix to the total turbulent energy scheme has been implemented to correct an issue introduced when porting from ECHAM to ICON, which caused excessive vertical diffusion in earlier model versions (Giorgetta et al., 2022; Franke and Giorgetta, 2024). This correction ensures a more realistic turbulent contribution to updraft velocity and thus cloud droplet activation.

To explore how CF sensitivity to aerosol perturbations is represented in ICON-HAM, we use N_d as a proxy for cloud-active aerosol, consistent with recent satellite-based studies (e.g. Gryspeerdt et al., 2016; Christensen et al., 2020; Chen et al., 2024). All simulations in this study follow the AMIP protocols, with sea-surface temperatures (SST) and sea ice prescribed from observations (Taylor et al., 2000). We conduct six simulations that pair two different cloud cover parameterization schemes with three different prescribed lower bounds for cloud droplet number concentration ($N_\mathrm{d,min}$). The following subsections detail the specific configurations of these simulations.

2.1.2 Cloud cover and autoconversion parameterization schemes

A central aspect of this study involves comparing two parameterizations for fractional cloud cover that fundamentally differ in whether cloud water directly controls cloud cover. Throughout this study, we refer to these schemes as CC-RH, which depends only on grid-mean RH, and CC-RH-LWC, which additionally depends on the total cloud water content.

CC-RH follows the implementation in the ECHAM6.3 general circulation model as described by Mauritsen et al. (2019), and is also the default configuration in ICON-HAM. In this scheme, CF is diagnosed as a function of grid-mean RH (Sundqvist et al., 1989):

$$\mathrm{CF} = 1 - \sqrt{1 - \frac{\mathrm{RH} - \mathrm{RH}_0}{1 - \mathrm{RH}_0}} \tag{1}$$

where RH_0 is a critical threshold RH specified as a function of height, as originally formulated in ECHAM4 (Roeckner et al., 1996). Clouds begin to form within a grid cell once RH_0 is exceeded. Further details on the parameter settings and tuning of CC-RH can be found in Mauritsen et al. (2019).

The CC-RH-LWC scheme follows the parameterization proposed by Xu and Randall (1996), previously referred to as COUPL-CC by Lohmann and Feichter (1997). In this scheme, CF increases with RH and additionally with the cloud water content q_w (the sum of liquid and ice water mixing ratios, which is predominantly liquid for MLCs) through an exponential factor:

$$\mathrm{CF} = \mathrm{RH}^{0.25}\left[1 - \exp\left(-250\left[(1-\mathrm{RH})q_{vs}\right]^{-0.45} q_w\right)\right] \tag{2}$$

with q_{vs} being the saturation specific humidity. The key distinction is that CC-RH-LWC explicitly depends on cloud water content, whereas CC-RH does not. This fundamental difference allows aerosol-induced changes in autoconversion and precipitation, which affect cloud water and hence LWP, to directly feed back on CF in CC-RH-LWC, a process that is absent in CC-RH.

All experiments use the autoconversion parameterization scheme of Khairoutdinov and Kogan (2000), derived from bin-resolving microphysics in large-eddy simulations (LES) of marine stratocumulus. Although originally developed for LES applications, it has been adopted in many GCMs. In what follows, this scheme is referred to as KK2000. The KK2000 autoconversion rate has a relatively strong inverse dependence on N_d ($N_\mathrm{d}^{-1.79}$), and it scales with cloud liquid water content, allowing for interactions with the cloud-cover schemes described above.

2.1.3 Prescribed $N_{\mathrm{d,min}}$

It is a common practice in global aerosol-climate models to impose $N_{\mathrm{d,min}}$ throughout the modelled atmosphere at all locations and altitudes. This constraint is typically imposed to avoid unrealistically low N_d values that may arise from the incomplete representation of natural background aerosol species that could contribute to CCN and N_d (e.g. nitrate and biological particles) (Kirkevåg et al., 2008), or from potential underprediction of specific aerosol sources (e.g. fine-mode sea salt) (Wang and Penner, 2009).

However, this practice is unphysical and the specific choice of the lower bound value is somewhat arbitrary. Hoose et al. (2009) systematically investigated the influence of these lower bounds and found that they can suppress the simulated aerosol indirect effect by up to 80 % by artificially creating more uniform N_d fields. By design, these N_d constraints are triggered more frequently where low N_d is more common, even though the observed N_d can drop well below the imposed threshold. This reduces the contrast between clean and polluted regimes. Consequently, under pre-industrial emissions the impact of prescribing $N_\mathrm{d,min}$ is comparably large over land and ocean, whereas under present-day emissions, it is most evident over oceans (Hoose et al., 2009).

Typical values of this lower bound have ranged between 5 and 40 cm^{-3} across different models (Hoose et al., 2009). ECHAM4 and ECHAM5 have used a $N_\mathrm{d,min}$ value of 40 cm^{-3} (Lohmann et al., 1999, 2007), and ECHAM6.3–HAM2.3 added an additional option of 10 cm^{-3} (Neubauer et al., 2019). In our study, in addition to 10 and 40 cm^{-3}, we also impose a more stringent $N_\mathrm{d,min}$ of 100 cm^{-3} to further examine how a prescribed minimum N_d interacts with CC-RH and CC-RH-LWC cloud cover schemes and modulates the CF sensitivity, yielding six experiments in total.

2.1.4 ICON-HAM output data as ML input

In this study, we apply an explainable ML framework similar to that used in J24 (described below in Sect. 2.2), where N_d along with large-scale meteorological fields are used to predict CF. The data used as input for the XGBoost models here are ICON-HAM model outputs. Predictors for the XGBoost models are listed in Table A1. To facilitate direct comparison with our MODIS-based study J24, we remapped ICON-HAM outputs on the native icosahedral grid to the MODIS $1^\circ \times 1^\circ$ latitude-longitude grid using nearest-neighbour interpolation. The original 47 vertical levels in ICON-HAM's hybrid sigma-height coordinate system were interpolated to six desired standard pressure levels (1000, 950, 900, 850, and 700 hPa) using conservative remapping. Owing to storage and computational constraints associated with producing global hourly output, the analysis is restricted to five years of data (2011–2015).

The low-level CF used here to approximate MLCs is diagnosed as the fractional cover of liquid clouds with cloud-top temperature warmer than 268 K, as viewed from the top of the atmosphere whenever high- and mid-level clouds were absent. This "unobscured" diagnostic is considered more suitable for analyzing drivers of liquid cloud cover, because the coarser resolution of ICON-HAM relative to MODIS increases the likelihood of overlying clouds masking the true extent of the low-level CF. Unlike our observational study (J24), where N_d was derived specifically for satellite retrievals from cloud droplet effective radius and cloud optical depth, here we use the model's instantaneous cloud-top, in-cloud N_d diagnostic. To improve comparability with J24, we apply analogous filtering criteria here: Low clouds must have a cloud-top temperature warmer than 268 K; cases with a cloud-top in-cloud effective radius smaller than 4 $\mathrm{\mu m}$ or a cloud optical depth smaller than 4 are excluded.

To characterize the dynamic and thermodynamic state of the atmosphere, the ML framework uses 23 meteorological variables in addition to $\ln N_\mathrm{d}$ as predictors in the ML model. This selection largely follows J24 except for several adaptations described below. A full list of predictors is provided in Table A1. We diagnose boundary-layer height (BLH) as the lowest model level at which the mean RH first drops below 50 %, following a standard LES-based proxy for the stratocumulus top and inversion height (Bretherton et al., 2013), which effectively captures the sharp transition from the moist boundary layer to the dry free troposphere above. This threshold has been used in a recent ICON-based analysis of stratocumulus adjustments and was shown to align well with the modelled cloud top (Fons et al., 2024). Convective available potential energy (CAPE) was dropped from the predictor set because it is primarily relevant for deep convective processes rather than for the stratiform

© Author(s) 2026. CC BY 4.0 License.

and shallow cumulus marine boundary-layer clouds that are the focus of this study. Moreover, in addition to RH at 700 and 850 hPa, we include two more lower pressure levels, 900 and 950 hPa, which are considered more relevant for MLCs.

Unlike J24, we do not standardize the predictor variables in this work. In J24, standardisation placed all predictors on a common and unitless scale to allow direct comparisons among all predictors with different units. However, our objective here is to compare the $\ln N_\mathrm{d}$–CF sensitivity across the six ICON-HAM configurations (two different cloud cover schemes and three $N_\mathrm{d,min}$ values), rather than to rank predictors by relative importance. We hence retain predictors on their native physical scales to preserve the interpretability of ICON-HAM's CF responses across six experiments in this study.

2.2 Explainable Machine Learning framework

2.2.1 Regional tree-based machine-learning models

We adopt the explainable machine learning framework from J24 to quantify the sensitivity of MLC CF to $\ln N_\mathrm{d}$ (proxy for aerosol) while accounting for meteorological covariability and confounding effects. A tree-based ensemble XGBoost algorithm (Chen and Guestrin, 2016) is employed due to its ability to capture nonlinear relationships and model feature interactions, while achieving high predictive performance with computational efficiency for tabular data. As in J24, an independent XGBoost model is trained within each $5^\circ \times 5^\circ$ geographical window to predict CF, using spatiotemporal samples aggregated from $1^\circ \times 1^\circ$ grid cells (remapped from native icosahedral grids) to capture regional characteristics and relationships.

For better comparability with our MODIS-based study (J24), we configure ICON-HAM to output hourly variables, then match them with MODIS Terra overpass times. The XGBoost models are trained on these outputs from 2011 to 2015 (Sect. 2.1.4. Unlike J24, where the train–test split was purely chronological, here we ensure that different climate states are represented in the training data. To sample distinct ENSO phases, we train the models on a La Niña year (2011), a neutral SST year (2013), and an El Niño year (2015), consistent with the documented ENSO conditions during these periods (Null, 2025). Model testing is performed on the intermediate years 2012 and 2014. The spatial patterns of annual SST anomalies relative to the five-year mean are shown in Fig. S1.

As in J24, hyperparameters for each regional XGBoost model are tuned via Bayesian optimization with five-fold cross-validation, and the number of boosting rounds is determined by early stopping to prevent overfitting. In this study, we expand the hyperparameter tuning to include XGBoost's complete family of column-wise subsampling hyperparameters *colsample_bylevel* and *colsample_bynode* in addition to *colsample_bytree* used in J24. These parameters control the fraction of features randomly selected at different stages of tree construction (per depth level, per node and per tree, respectively). With these subsampling parameters, the XGBoost model tends to spread feature importance more evenly across correlated features. In this way, we could prevent unphysical overfitting to any single predictor and obtain more robust SHAP attributions that reflect the collective influence of intercorrelated variables. The XGBoost models from J24 were re-tuned in this study based on this more comprehensive hyperparameter set. Thus, the MODIS-based results presented here are marginally different from those reported in J24.

https://doi.org/10.5194/egusphere-2026-569
Preprint. Discussion started: 20 February 2026
© Author(s) 2026. CC BY 4.0 License.

2.2.2 Explaining the machine-learning models

The SHAP approach is used to explain the regional XGBoost models. SHAP provides additive, local attributions of each predictor to the CF prediction (Lundberg et al., 2018, 2020). SHAP decomposes every individual prediction into a base value and contributions from each feature, allowing the specific influence of $\ln N_\mathrm{d}$ on CF to be isolated while accounting for the influences of meteorological covariates. The SHAP base value is what the model would predict with no feature information (Lundberg and Lee, 2017), typically calculated as the average prediction over the entire training set. Positive (negative) SHAP values indicate that a predictor raises (lowers) the prediction relative to this baseline. In our framework, the SHAP base value can be interpreted as the climatological mean CF over the training dataset in a given geographical window, representing the expected XGBoost prediction given the mean state of meteorology and N_d. Each feature's SHAP value then quantifies the magnitude and direction (positive or negative) that the specific feature value contributes to the CF prediction, shifting the final prediction away from this mean baseline. By construction, the sum of all SHAP values plus the base value equals the final prediction of the model, ensuring additivity and consistency.

Following J24, plotting SHAP values of $\ln N_\mathrm{d}$ against its feature values yields a SHAP dependence plot where the slope is taken as the $\ln N_\mathrm{d}$–CF sensitivity for a given geographical window. For the ICON-HAM analysis, however, a methodological adaptation is required: instead of a single linear regression fit, piecewise linear regression (PLR) is applied. This choice is motivated by the stronger nonlinear (saturating) behaviour in the ICON-HAM–based $\ln N_\mathrm{d}$–CF relationships compared with those in J24. In ICON-HAM, the CF response to $\ln N_\mathrm{d}$ diminishes at higher $\ln N_\mathrm{d}$ even after the logarithmic transformation, reflecting a saturation effect that largely disappeared after log transformation in J24. The PLR approach retains comparability to J24's method while allowing the nonlinearities to be captured. A complete overview of the XGBoost+SHAP global framework is provided in J24. Further details on the ICON-HAM nonlinearities and rationale for PLR are discussed in Sect. 3.2, and the breakpoint selection strategies for data segmentation are detailed in Sect. 2.3 and Appendix B.

2.3 Piecewise linear regression with constraint-aware breakpoints

Here we introduce a constraint-aware breakpoint with fixed interval in logarithmic space, which is the primary strategy used in our main analysis. Specifically, it is called "constraint-aware" because it defines the breakpoint relative to the prescribed minimal constraint on cloud droplet number ($N_\mathrm{d,min}$). This strategy sets the fixed interval between $N_\mathrm{d,min}$ and the breakpoint directly in the predictor space of $\ln N_\mathrm{d}$:

$$\ln(N_\mathrm{d,bp}) = \ln(\mathrm{N_{d,min}}) + \delta \tag{3}$$

where $N_\mathrm{d,bp}$ denotes the breakpoint and δ represents the logarithmic offset from the imposed lower bound. In linear space this gives $N_\mathrm{d,bp} = \mathrm{N_{d,min}} \times e^{\delta}$. In this study, we fix the log-space interval $\delta = 0.1$, so $N_\mathrm{d,bp} \approx \mathrm{N_{d,min}} \times 1.105$, yielding breakpoints of approximately 11, 44, and 111 $\mathrm{cm^{-3}}$ for the $N_\mathrm{d,min}$ = 10, 40, and 100 $\mathrm{cm^{-3}}$ experiments, respectively. Using a constant increment in logarithmic space enforces the same relative (multiplicative) distance from $N_\mathrm{d,min}$ across all experiments and

https://doi.org/10.5194/egusphere-2026-569
Preprint. Discussion started: 20 February 2026
© Author(s) 2026. CC BY 4.0 License.

is consistent with logarithmic scaling of the $\ln N_\mathrm{d}$ predictor. By placing the breakpoints ∼10.5% above the imposed lower bounds, this approach is designed to effectively capture the transition from a regime controlled by the lower bound, and a regime free from the lower bound.

This PLR framework is applied to the $\ln N_\mathrm{d}$ SHAP dependence plots for each $5° \times 5°$ geographical window. Data are segmented at the identified breakpoint, and separate linear regressions are fitted for the below- and above-breakpoint regimes to yield slopes β_b and β_a, respectively. For numerical stability, we require at least 1000 data points in the below-breakpoint regime and 500 in the above-breakpoint regime for each geographical window. A detailed visual demonstration of this PLR approach applied to an exemplary geographical window is presented later in Sect. 3.3.1. To assess robustness, we test two alternative breakpoint strategies: a constraint-aware approach with fixed intervals in linear space, and a statistically optimized approach that minimizes fitting error within a constraint-aware search range. These two alternative strategies and their results are detailed in Appendix B.

3 Results and discussion

3.1 Mean states of marine low clouds in ICON-HAM

Here we present how imposing lower-bound constraints of 10, 40 and 100 cm^{-3} elicits distinct responses in precipitation, liquid water in clouds, and cloud cover across the two cloud cover parameterization schemes (CC-RH and CC-RH-LWC). Figure 1 presents the global distributions of the mean precipitation rate at the surface (PR), LWP and CF for each $5° \times 5°$ geographical window.

As $N_\mathrm{d,min}$ increases, autoconversion is suppressed, leading to a reduction in the large-scale precipitation (Fig. 1a). This arises because higher $N_\mathrm{d,min}$ yields clouds populated by more numerous and smaller droplets, which is less favourable for drizzle formation. The KK2000 autoconversion scheme captures this effect through its relatively strong inverse dependence on N_d (Khairoutdinov and Kogan, 2000). Even the cleanest clouds within each experiment (with N_d at or slightly above $N_\mathrm{d,min}$) become inefficient in producing rain, allowing more water to accumulate in the clouds and thus resulting in higher LWP (Fig. 1b). We see that PR decreases from $N_\mathrm{d,min}$ = 10 to 40 cm^{-3} and then levels off, while LWP continues to increase throughout the entire range. This decoupling occurs because the LWP represents a reservoir of cloud water, whereas PR is a flux at the surface. Weakening the internal cloud process of autoconversion directly helps build up the reservoir, but changes in its level do not necessarily scale with changes in the surface flux. Moreover, PR is balanced by surface evaporation, which is mainly governed by surface energy budget and hence by surface temperature (Held and Soden, 2006). Since SSTs are prescribed in our AMIP simulations, oceanic evaporation is relatively constrained, limiting and converging PR changes.

By construction, the two cloud-cover schemes produce contrasting CF responses. In CC-RH-LWC, the explicit dependence of CF on cloud water content means the rising LWP at high $N_\mathrm{d,min}$ translates directly into a steady increase in CF. Meanwhile, CC-RH, relying solely on grid-mean RH, shows a decline followed by a plateau that mirrors the PR trend. This behaviour likely results from higher $N_\mathrm{d,min}$ leading to smaller droplets and suppressed precipitation formation. Smaller droplets reduce sedimentation and also evaporate faster at the cloud top, enhancing cloud-top entrainment. Meanwhile, less drizzle evaporates

© Author(s) 2026. CC BY 4.0 License.

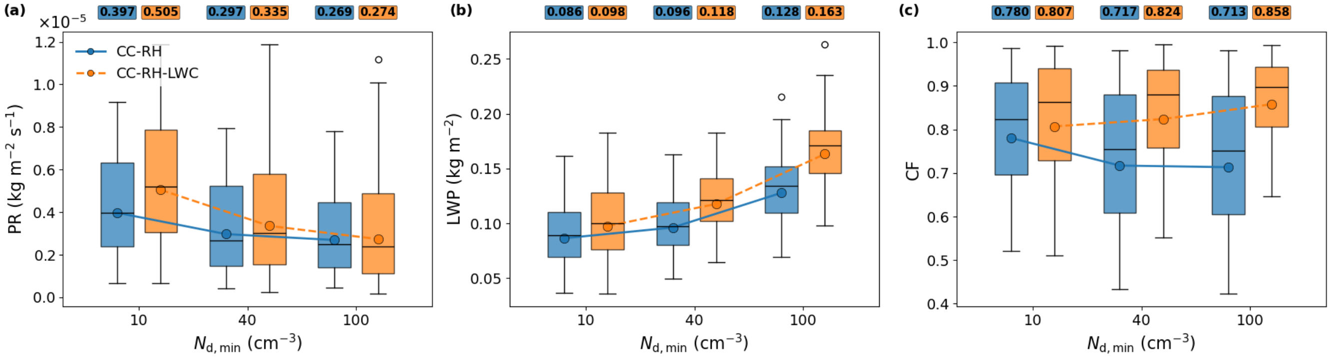

Figure 1. Distributions of $5^\circ \times 5^\circ$ geographical-window-mean precipitation rate (PR; panel a), liquid water path (LWP; panel b) and cloud fraction (CF; panel c) over the global oceans for marine liquid clouds during 2011–2015. The simulations compare two cloud cover parameterization schemes (CC-RH and CC-RH-LWC) and three imposed minima of cloud droplet number concentration ($N_{\mathrm{d,min}}$ = 10, 40, 100 cm^{-3}). Each window's value is the spatiotemporal mean of the aggregated $1^\circ \times 1^\circ$ grid cells. The blue boxes and solid lines represent the results from the CC-RH scheme, while the orange boxes and dashed lines represent the CC-RH-LWC scheme. Each box shows the interquartile range. Whiskers expand the boxes by up to 1.5 interquartile ranges, and individual points are outliers. Median values are represented by the horizontal lines, while the global area-weighted mean values are represented by circular markers and overlaid lines.

below the cloud and more condensate is retained in the cloud layer, diminishing sub-cloud evaporative moistening. Both act to lower grid-mean RH. While similar drying can occur in CC-RH-LWC, it is offset by the LWP-driven CF increase, yielding an overall rise in cloud cover.

The stronger increase in mean-state CF with the higher artificial N_{d} floor seen in CC-RH-LWC (relative to CC-RH) is qualitatively consistent with Lohmann and Feichter (1997). In their study, when aerosol loading increased from preindustrial (PI) to present-day (PD), the cloud-water-dependent scheme (the same as our CC-RH-LWC) showed a roughly 3 % CF increase under elevated aerosol emission levels, compared with only about 1 % in their RH-only scheme (conceptually similar to our CC-RH). Although their mechanisms differ from ours (emission changes versus prescribed lower bounds), both approaches show that CC-RH-LWC's explicit dependence on cloud water content amplifies the CF response when autoconversion is suppressed by increased N_{d} and liquid water accumulates. We therefore interpret the divergence between schemes in Fig. 1c as consistent in sign with Lohmann and Feichter (1997), even though $N_{\mathrm{d,min}}$ experiments are not perfect PI and PD analogues. This supports the view that the pronounced CF response in CC-RH-LWC stems from its direct coupling between cloud cover and liquid water, which becomes particularly evident when autoconversion is weakened due to autoconversion's dependence on droplet number, which $N_{\mathrm{d,min}}$ directly affects.

3.2 Observations vs. default ICON-HAM setup using one linear regression

We first compare the CF sensitivity to $\ln N_{\mathrm{d}}$ globally based on the ICON-HAM default model setup (CC-RH cloud cover parameterization with $N_{\mathrm{d,min}}$ = 40 cm^{-3}) to that of the observational results of J24. The sensitivities here are quantified

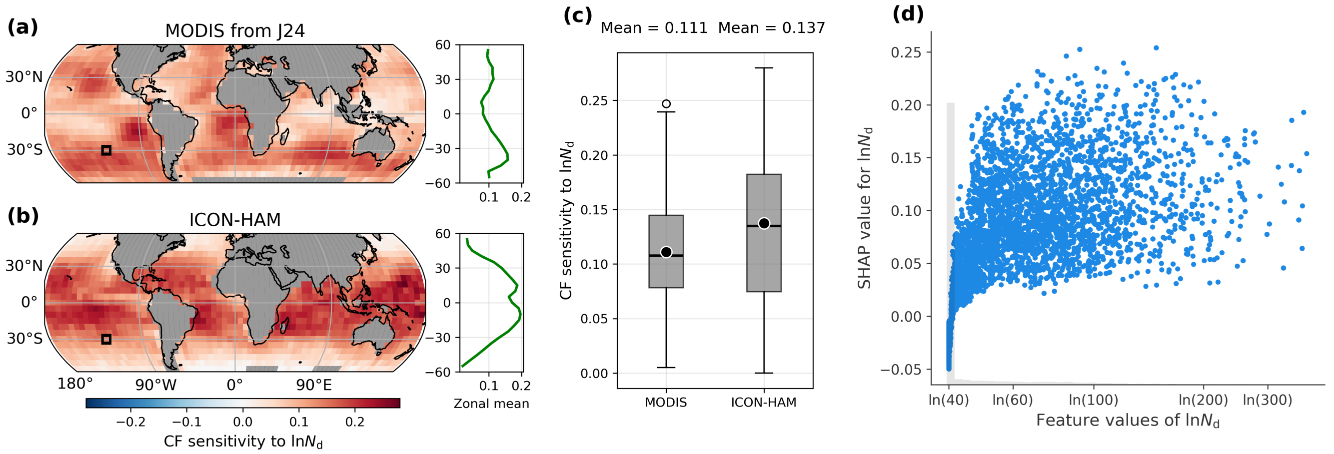

Figure 2. Comparison of marine low-cloud fraction (CF) sensitivity to log-transformed cloud-droplet number concentration ($\ln N_\mathrm{d}$) between MODIS-based results from J24 (recomputed here with retrained XGBoost models using extended column-wise subsampling hyperparameters; see Sect. 2.2.1) and ICON-HAM simulations using the default CC-RH cloud-cover scheme with $N_\mathrm{d,min}$ = 40 cm^{-3}. Panels (a) and (b) show spatial patterns and zonal means of the observed and modelled $\ln N_\mathrm{d}$–CF sensitivities, respectively. (c) Distributions of the CF sensitivities; thick black lines denote medians, and black dots show area-weighted global means (values above boxes). (d) ICON-HAM SHAP dependence plot for $\ln N_\mathrm{d}$ in the exemplary geographical window at 27.5°–32.5°S, 122.5°–127.5°W, whose location is marked by squares in panels (a) and (b). Grey bars in the background indicate the distribution of $\ln N_\mathrm{d}$ feature values.

following the approach in J24, defined as the slope derived from an ordinary least-squares linear regression of the $\ln N_\mathrm{d}$ SHAP values against the $\ln N_\mathrm{d}$ feature values for each $5° \times 5°$ geographical window.

MODIS-based results (Fig. 2a) show more spatially heterogeneous CF sensitivities, strongest in the stratus-to-cumulus transition regions off western coasts and in the Southern Hemispheric midlatitudes. In contrast, ICON-HAM displays more widespread and contiguous areas of high $\ln N_\mathrm{d}$–CF sensitivity, pronounced over nearly all subtropical regions, including stratocumulus regions, trade cumulus regions, and tropical ascending regions (Fig. 2b). Unlike MODIS results, the regions with the strongest sensitivities in the Pacific and Atlantic Oceans are located more westward, away from the west coasts. Zonal means show that both ICON-HAM and MODIS exhibit weaker sensitivities near the equator compared to subtropical regions, likely reflecting the greater dominance of deep convection and strong meteorological variability in the tropics. These dynamical factors limit the prevalence of stratiform liquid clouds and obscure the signal of aerosol-CF relationships compared to the extensive subtropical stratocumulus decks. Another major difference appears in the Southern Hemispheric midlatitudes, where ICON-HAM shows weak sensitivities. The geographic differences in sensitivity patterns suggest that key controlling processes may differ between observations and ICON-HAM, notably regions where the model frequently computes shallow convection. For instance, differences in droplet size distributions can alter entrainment-evaporation feedbacks and precipitation efficiency, thereby shifting the spatial pattern of the sensitivity.

© Author(s) 2026. CC BY 4.0 License.

The distributions of the CF sensitivity values (Fig. 2c) show that the global weighted mean sensitivities are of similar magnitude in ICON-HAM (0.137) and MODIS (0.111), with ICON-HAM being somewhat higher and exhibiting greater variability. Note the value of 0.111 differs slightly from that reported in J24 because XGBoost models were re-tuned using the more comprehensive hyperparameters in this study (Table A1). The global weighted mean value of ICON-HAM is similar to the MODIS-based estimate but higher than the values reported for other GCMs including ECHAM (Wang et al., 2025). This does not necessarily contradict the broader expectation discussed in the Introduction that models tend to underestimate aerosol–cloud forcing relative to observation-based constraints, as the sensitivity does not translate directly to radiative forcing. However, the larger simulated sensitivities motivate further investigation of their origin (e.g. at individual geographical window) and of potential methodological limitations when applying SHAP with a single linear regression for ICON-HAM.

In light of this, we examine the relationship between predicted CF and $\ln N_\mathrm{d}$ in the same exemplary geographical window as in J24 (Fig. 2d). The ICON-HAM relationship is clearly not as linear as the one based on MODIS. The cloud cover saturation effect, or the dependence of cloud cover sensitivity on background N_d, has already been documented: CF increases quickly with increasing N_d, but the rate of increase approaches zero after reaching an N_d threshold at approximately 60 cm^{-3} (e.g. Hu et al., 2021; Yuan et al., 2023). This effect can be reflected by a sharply decreasing derivative (dCF/dN_d in Yuan et al. (2023) or dSHAP/dN_d in J24) before the saturation threshold and a nearly flattened curve after the threshold is exceeded.

As shown in J24, using MODIS data, this effect only manifests evidently as a nonlinear relationship between the N_d feature values and their corresponding SHAP values, which becomes much more linear after applying a logarithmic transformation to N_d. In ICON-HAM data for the same geographical window, the relationship remains strongly nonlinear and the CF saturation effect persists even after the logarithmic transformation (Fig. 2d). This more nonlinear CF response in ICON-HAM likely arises because ICON-HAM's cloud-cover and microphysics schemes are formulated based on process-level understanding of the small-scale nonlinearities observed, for example, in field campaigns (Lohmann and Feichter, 1997) and LES constrained by such field campaigns (Khairoutdinov and Kogan, 2000). At these small scales, cloud systems can shift abruptly once critical thresholds are crossed, resulting in step-like responses. Since these parameterizations include physical constraints such as thresholds and saturation limits, the resulting model output retains its inherent nonlinearity, and this signature of its core physics persists even after aggregation from $1^\circ \times 1^\circ$ grid cells to $5^\circ \times 5^\circ$ geographical windows.

At larger scales, by contrast, the abrupt CF responses that arise from microphysical thresholds are smoothed out. This occurs because higher aerosol concentrations delay the breakup of cloud decks, prolonging their lifetime. As winds advect these systems, the temporal delay in cloud dissipation allows cloud cover to persist over a longer track, which effectively translates into a spatial extension of cloudiness. Consequently, under spatial aggregation across many sampled cloud scenes, a larger fraction of the sampled domain remains cloudy, the spatially aggregated CF response appears gradual and more linear (Goren et al., 2019, 2022; Rosenfeld et al., 2023). This linearity is precisely the characteristic behaviour observed in large-scale satellite analyses, including our previous MODIS-based study (J24).

The simple linear regression between SHAP values and feature values of $\ln N_\mathrm{d}$ used in J24 to quantify the $\ln N_\mathrm{d}$–CF sensitivity is not suitable for ICON-HAM output, where the relationships are strongly nonlinear. To account for these while maintaining comparability with J24's methodology and other linear sensitivity estimates, we apply the PLR approach with a breakpoint strategy defined in Sect. 2.3, similar in spirit to the segmented fitting approach applied to the nonlinear N_d –LWP relationships by Gryspeerdt et al. (2019). This breakpoint strategy ensures a consistent proportional offset from the imposed lower bounds across all simulations, which is more appropriate given the logarithmic nature of the $\ln N_\mathrm{d}$ predictor. Physically, this approach is intended to effectively capture the transition from a near-$N_\mathrm{d,min}$ (lower-bound-constrained) regime with strong CF sensitivity to $\ln N_\mathrm{d}$ to a high N_d regime with a weaker CF response. To illustrate how this strategy operates with PLR based on SHAP dependence plots, we zoom in on the SHAP dependence for all six simulations in the same exemplary geographical window as Fig. 2d; the detailed visualization and discussions are provided in Sect. 3.3.1.

To assess the influence of breakpoint selection on our results, we evaluated two additional strategies beyond the default strategy described above. The first is an alternative constraint-aware approach with a fixed interval on a linear scale of 5 cm^{-3} (Appendix B1). The second is a data-driven approach where the breakpoint is statistically optimized within a constrained search range extending 50 cm^{-3} above each $N_\mathrm{d,min}$ value (Appendix B2). This hybrid design combines statistical data-driven flexibility with the $N_\mathrm{d,min}$ constraints. The full methodology and global results for these alternative strategies are presented in Appendix B.

3.3 From ICON-HAM physical states to SHAP-detected sensitivity: the headroom mechanism

3.3.1 Piecewise sensitivity and headroom effect at the exemplary geographical window

Figure 3 illustrates the application of PLR with constraint-aware breakpoints $\ln(N_\mathrm{d,bp}) = \ln(\mathrm{N_{d,min}}) + 0.1$ at the exemplary geographical window. The panels confirm the pronounced nonlinearity in the $\ln N_\mathrm{d}$–CF relationship, which justifies our piecewise approach. First, the slopes on either side of the breakpoint (vertical coloured dashed lines) contrast systematically: the below-breakpoint regime has a stronger sensitivity (β_b) than the above-breakpoint regime (β_a) across all experiments. The summary panels (d) and (h) make the two regimes and the associated saturation effect visually explicit. Second, regime occupancy shifts with $N_\mathrm{d,min}$ and gets markedly asymmetric at high $N_\mathrm{d,min}$: At $N_\mathrm{d,min}$ = 10 cm^{-3}, samples are split roughly evenly between the two regimes. However, at 40 and 100 cm^{-3}, the vast majority fall below the breakpoint, with the below-breakpoint fraction increasing with $N_\mathrm{d,min}$, reflecting that more data are truncated by the higher $N_\mathrm{d,min}$ constraints and thus concentrated near the imposed bounds.

The below-breakpoint slopes vary systematically with both $N_\mathrm{d,min}$ and cloud-cover scheme, whereas the above-breakpoint slopes remain broadly comparable. At $N_\mathrm{d,min}$ = 10 cm^{-3}, CC-RH-LWC shows a larger β_b than CC-RH. For CC-RH, β_b increases from 10 to 40 cm^{-3} and then decreases from 40 to 100 cm^{-3} with the magnitudes at 40 and 100 cm^{-3} remaining comparable. By contrast, β_b in CC-RH-LWC declines drastically as $N_\mathrm{d,min}$ increases, despite its explicit dependence on cloud water content. Consequently, β_b is weaker in CC-RH-LWC than CC-RH at higher $N_\mathrm{d,min}$. This apparent paradox reflects a “headroom effect”, more visible when viewing the pattern against the secondary y-axes for predicted CF (Fig. 3): At high $N_\mathrm{d,min}$, CC-RH-LWC already attains a substantially elevated baseline CF (given by the SHAP base values indicated by the horizontal black solid lines). Therefore, CF predictions approach the physical ceiling of 1.0, and the marginal sensitivity to

https://doi.org/10.5194/egusphere-2026-569
Preprint. Discussion started: 20 February 2026
© Author(s) 2026. CC BY 4.0 License.

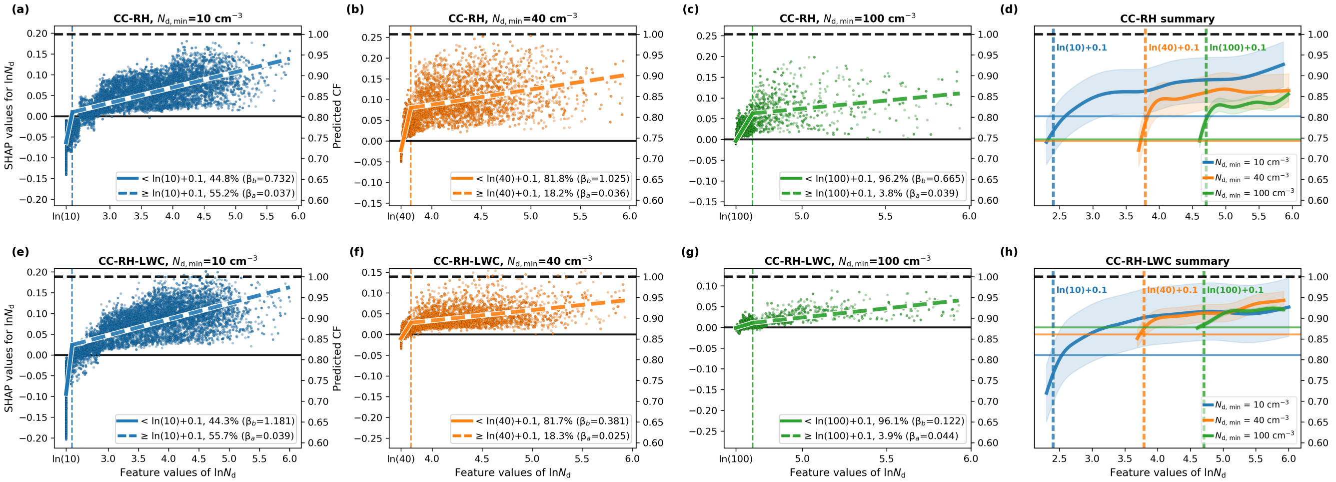

Figure 3. SHAP dependence plots for log-transformed cloud droplet number concentration ($\ln N_\mathrm{d}$) at the exemplary geographical window (27.5°-32.5°S, 122.5°-127.5°W) for six ICON-HAM simulations. Top row (a–d): the CC-RH scheme; bottom row (e–h): the CC-RH-LWC scheme. Columns correspond to $N_\mathrm{d,min}$ values of 10, 40 and 100 cm^{-3} (left to right). In panels (a–c) and (e–g), the x-axis shows feature values of $\ln N_\mathrm{d}$, and the primary y-axis shows SHAP values for $\ln N_\mathrm{d}$. The secondary y-axis (right) shows XGBoost-predicted CF (SHAP values + SHAP base value). Horizontal solid black lines indicate zero SHAP contribution on the primary axis and the baseline CF prediction on the secondary axis; the horizontal dashed line marks CF = 1.0. To quantify $\ln N_\mathrm{d}$–CF sensitivity, piecewise linear regression (PLR) is applied with a single breakpoint at $\ln(N_\mathrm{d,bp}) = \ln(\mathrm{N_{d,min}}) + 0.1$. Solid and dashed regression lines show the fitted slopes below (β_b) and above (β_a) the breakpoint, respectively. Vertical dashed lines indicate breakpoint locations. Percentage values in the legend report the fraction of samples in each regime. Panels (d) and (h) summarize the CC-RH and CC-RH-LWC results, respectively, using generalized additive model fits with 95 % prediction intervals. Colours match corresponding scatter plots.

further $\ln N_\mathrm{d}$ increases diminish due to saturation. In contrast, CC-RH maintains lower baseline CF values, preserving a greater dynamic range for $\ln N_\mathrm{d}$ to influence CF.

This SHAP-based piecewise approach effectively captures an intrinsic ICON-HAM behaviour in the $\ln N_\mathrm{d}$–CF relationships: a transition from a steeper, $N_\mathrm{d,min}$-constrained regime to a flatter, far-from-$N_\mathrm{d,min}$ regime. Although the interval between the breakpoint and $N_\mathrm{d,min}$ is fixed in log space across all experiments, the fraction of data points in the first regime increases with $N_\mathrm{d,min}$, consistent with stronger truncation and tighter constraint near the higher imposed lower bounds. A clear headroom trend emerges: the baseline CF is higher in CC-RH-LWC and increases further with $N_\mathrm{d,min}$, leaving less room for additional CF gains and thus dampening the sensitivity.

3.3.2 Global patterns of SHAP base values and mean absolute SHAP of $\ln N_\mathrm{d}$

Section 3.1 showed that imposing higher $N_\mathrm{d,min}$ values suppresses autoconversion and drizzle, leading to reduced PR and enhanced LWP in both cloud-cover schemes. In CC-RH-LWC, where CF depends explicitly on cloud water, higher LWP directly translates into higher CF, resulting in a mean state characterized by more extensive cloud decks. Conversely, CC-RH, which depends solely on RH, shows little change or even a decline in CF, likely driven by reduced grid-mean RH associated with enhanced cloud-top entrainment and weaker sub-cloud evaporative moistening. As a result, at $N_{\mathrm{d,min}}$ = 40 and 100 cm^{-3}, the two schemes produce markedly different baseline CF states, consistent with the behaviour reported by Lohmann and Feichter (1997). In the following, we examine how these mean-state differences are reflected in the SHAP base values and mean absolute SHAP values of $\ln N_{\mathrm{d}}$, which together describe the baseline cloud state and the overall contribution strength of aerosol variability within the SHAP framework.

Figure 4 zooms out from the exemplary window to place this behaviour in a global context. Figure 4a presents the global distribution of SHAP base values. Defined as the average of all XGBoost predictions over the training set, the SHAP base value corresponds directly to the local climatological mean-state CF. Indeed, their global distributions resemble the contrasting behaviours of CC-RH and CC-RH-LWC observed in Fig. 1c. In other words, variations in SHAP base values across experiments primarily indicate the physical shifts in the simulated CF mean state attributed to the influence of $N_{\mathrm{d,min}}$ on autoconversion and drizzle.

Panel (b) shows the global distribution of the mean absolute SHAP value for $\ln N_{\mathrm{d}}$, which is a measure of its feature importance or average marginal contribution. At 10 cm^{-3}, $\ln N_{\mathrm{d}}$ shows greater feature importance in CC-RH-LWC than in CC-RH, reflecting CC-RH-LWC's direct CF-LWC coupling, which enables Nd-induced liquid water changes to immediately affect cloud cover. At $N_{\mathrm{d,min}}$ = 40 and 100 cm^{-3}, the opposite holds: CC-RH has a larger $\ln N_{\mathrm{d}}$ contribution, since there is limited headroom for $\ln N_{\mathrm{d}}$ variability to drive further CF increases in CC-RH-LWC, constraining the marginal $\ln N_{\mathrm{d}}$ contributions. This global behaviour mirrors the headroom effect identified at the exemplary window in Sect. 3.3.1.

In summary, the influence of the differing treatment of liquid-water dependence is twofold both locally and globally: First, it alters the physical mean-state CF (the SHAP base value), and second, this baseline difference makes the system "headroom-mediated" by limiting the room for $\ln N_{\mathrm{d}}$ to contribute to CF increases. This twofold effect is also the key to explaining the resulting sensitivity patterns.

3.3.3 Global distribution of $\ln N_{\mathrm{d}}$–CF sensitivity

Having established how elevated SHAP base values (baseline CF) constrain the feature importance of $\ln N_{\mathrm{d}}$ within the SHAP framework, we now examine how this mechanism manifests itself in the global distribution of $\ln N_{\mathrm{d}}$–CF sensitivities derived from the PLR with the same breakpoint strategy (Sect. 2.3). The PLR slopes represent the directional sensitivity of CF to $\ln N_{\mathrm{d}}$. Accordingly, lower mean absolute SHAP values, which indicate weaker marginal contributions, naturally correspond to flatter PLR slopes since the individual SHAP values entering the regression are smaller in magnitude. This leads to flatter SHAP dependence plots when $\ln N_{\mathrm{d}}$ has limited capacity to contribute to CF predictions. Figure 5 summarizes the resulting global distributions of PLR-derived $\ln N_{\mathrm{d}}$ –CF sensitivities for the below- and above-breakpoint regimes. Consistently, the global distribution of the mean absolute SHAP values for $\ln N_{\mathrm{d}}$ (Figs. 4b) resembles that of the below-breakpoint sensitivities (Fig. 5a).

Across all experiments, the below-breakpoint sensitivities are systematically larger than the above-breakpoint ones, typically by about an order of magnitude (note the different y-axis ranges in Fig. 5a and b). The below-breakpoint regime reveals the

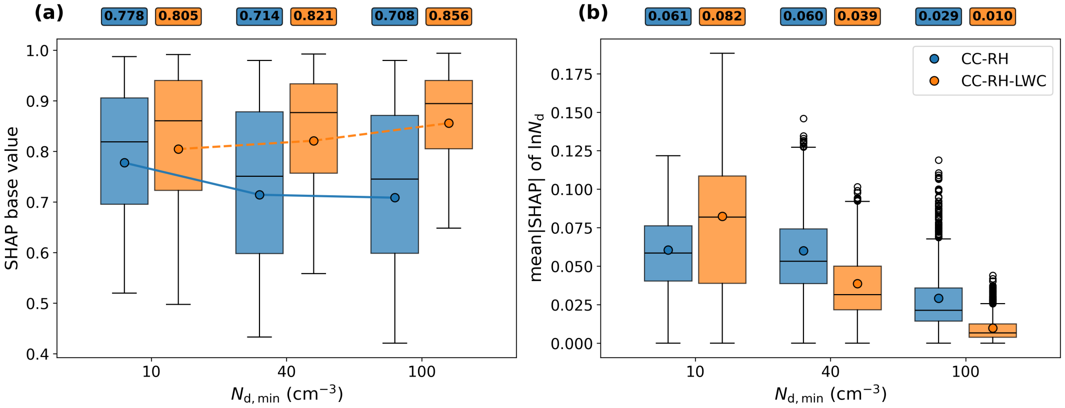

Figure 4. Global distributions of per-5° × 5°-window (a) SHAP base values for the prediction of CF and (b) mean absolute SHAP value of $\ln N_\mathrm{d}$ (feature importance) for global marine liquid clouds during 2011–2015, including six experiments (two cloud-cover schemes: CC–RH and CC–RH–LWC; three imposed N_d lower bounds, $\mathrm{N}_{\mathrm{d,min}} = 10, 40, 100\ \mathrm{cm}^{-3}$). Box plots show the interquartile range (IQR), whiskers extend to $1.5 \times \mathrm{IQR}$, circles denote outliers, and horizontal lines indicate medians. Global area-weighted means are shown as circular markers connected by lines, with the corresponding values annotated above each panel.

clearest inter-scheme contrasts and directly reflects the headroom mechanism described above. At $N_{\mathrm{d,min}}$ = 10 cm^{-3}, CC-RH-LWC shows stronger sensitivities than CC-RH (global area-weighted means of approximately 1.092 and 0.424, respectively). In line with Fig. 4, at this low $N_{\mathrm{d,min}}$, both schemes have similar baseline CF (and hence similar headroom), allowing CC-RH-LWC's explicit dependence on cloud liquid water to be fully expressed as both stronger feature importance and stronger derived CF sensitivity.

However, as $N_{\mathrm{d,min}}$ increases to 40 and 100 cm^{-3}, the pattern reverses. The global weighted means for CC-RH (approximately 1.135 and 1.011, respectively) exceed those of CC-RH-LWC (0.633 and 0.209, respectively). This systematic weakening in CC-RH-LWC aligns precisely with the SHAP diagnostics in Fig.4: the liquid-water-dependent scheme's high baseline CF (SHAP base values exceeding 0.85 at $N_{\mathrm{d,min}}$ = 100cm^{-3}) leaves minimal dynamic range for $\ln N_\mathrm{d}$ to act, thereby muting the marginal contribution captured by SHAP and leading to weaker PLR-derived sensitivities. Conversely, CC-RH maintains lower baseline CFs, preserving a larger dynamic range for $\ln N_\mathrm{d}$ to act, enabling stronger detected sensitivities.

Above the breakpoint, sensitivities are roughly an order of magnitude weaker than below it, and are centred near zero for both schemes (Fig. 5b). This attenuation mirrors the flatter upper segments of the SHAP dependence plots after saturation. In this regime, sensitivities remain relatively stable across $N_{\mathrm{d,min}}$ values (0.036–0.054 per unit $\ln N_\mathrm{d}$), and inter-scheme differences are minimal. This suggests that once $\ln N_\mathrm{d}$ values are high and less influenced by the imposed lower bounds, both parameterizations respond similarly weak to aerosol variability.

Taken together with Sect. 3.3.2, the counterintuitive finding of weaker $\ln N_\mathrm{d}$–CF sensitivities in CC-RH-LWC at high $N_{\mathrm{d,min}}$ does not indicate that its explicit CF–LWC coupling is ineffective. Instead, it demonstrates that the liquid-water dependence raises baseline CF and accelerates saturation, thereby diminishing the marginal contribution of $\ln N_\mathrm{d}$ and the sensitivity de-

© Author(s) 2026. CC BY 4.0 License.

tected by SHAP. This reflects a fundamental distinction between physical responsiveness and methodological detectability. In this sense, the global sensitivity patterns are "headroom-mediated", providing a coherent bridge from ICON-HAM's physical representation of cloud cover to the explainable-ML diagnostics.

A direct comparison with the MODIS-based results from J24 highlights the structural differences between observation- and model-based sensitivities. The global area-weighted mean sensitivity from J24, derived from a single linear regression, is approximately 0.111 (Fig. 2c). This value lies between our two PLR regimes: substantially smaller than the below-breakpoint means (0.209 to 1.135) but larger than the above-breakpoint means (0.036 to 0.054). This intermediate value falls between the two regimes and can be effectively interpreted as an aggregated response. However, the distinct segmentation and spread in ICON-HAM sensitivities indicate that the simulated sensitivity estimates are tricky and also dictated by model configuration and methodological choices, complicating direct model-observation comparisons and aerosol-cloud forcing estimates.

3.3.4 Robustness of findings and physical plausibility of breakpoints

To ensure our main findings are not an artefact of our primary breakpoint definition $\ln(N_{\mathrm{d,bp}}) = \ln(\mathrm{N}_{\mathrm{d,min}}) + 0.1$, we tested additional strategies: an alternative constraint-aware strategy with a fixed interval in linear space ($N_{\mathrm{d,min}}$ + 5 cm^{-3}, Sect.B1), and a statistically optimized constraint-aware approach that determines breakpoints by minimizing the overall fitting error within a search range constrained by $N_{\mathrm{d,min}}$ (Sect.B2). Despite differences in their underlying rationale and implementation, all three strategies yield qualitatively consistent results. First, the $\ln N_{\mathrm{d}}$–CF sensitivity in CC-RH-LWC is stronger at $N_{\mathrm{d,min}}$ = 10 cm^{-3} but becomes weaker than in CC-RH at 40 and 100 cm^{-3}. Second, inter-scheme differences are dominated by the below-breakpoint regime. This confirms the headroom mechanism independently of the specific breakpoint definition.

Beyond methodological consistency, the robustness of our findings is further supported by the physical plausibility of the breakpoint locations themselves. Independent observational studies of MLCs, using opportunistic experiments (ship tracks and volcanic eruptions) and large-scale satellite data (Hu et al., 2021; Yuan et al., 2023; Wang et al., 2024; Jia et al., 2024), have repeatedly identified a saturation threshold for CF responses to N_{d} at roughly 50–60 cm^{-3}. In addition, stratocumulus clouds are also known to transition from closed to open cells at a similar N_{d} threshold (Rosenfeld et al., 2023). In ICON-HAM, the breakpoint locations depend on the imposed $N_{\mathrm{d,min}}$ by design. For the default $N_{\mathrm{d,min}}$ of 40 cm^{-3}, however, they consistently fall close to the observational threshold range across three independently derived breakpoint strategies. The two constraint-aware strategies (Sect. 2.3 and B1) yield breakpoints of approximately 44 cm^{-3} and 45 cm^{-3}, respectively. Notably, the statistically optimized strategy (Sect. B2) independently finds a global area-weighted mean breakpoint value of about 48 cm^{-3} for CC-RH and 56 cm^{-3} for CC-RH-LWC (Fig. B4), closely matching the observed saturation threshold of $\sim$50–60 cm^{-3}). By contrast, the $N_{\mathrm{d,min}}$ = 10 cm^{-3} and 100 cm^{-3} experiments produce different breakpoint locations. The agreement for $N_{\mathrm{d,min}}$ = 40 cm^{-3} therefore suggests that this lower bound choice places the model's emergent onset of the CF saturation at a more physically plausible N_{d} level than the more extreme $N_{\mathrm{d,min}}$ settings.

Overall, the consistency of the breakpoint values among the three breakpoint-selection strategies, combined with agreement between the resulting breakpoints and the known range of the physical saturation thresholds in the $N_{\mathrm{d,min}}$ = 40 cm^{-3} simulations, confirms the robustness of our SHAP-based PLR approach and validates the underlying nonlinearity. This shows that the

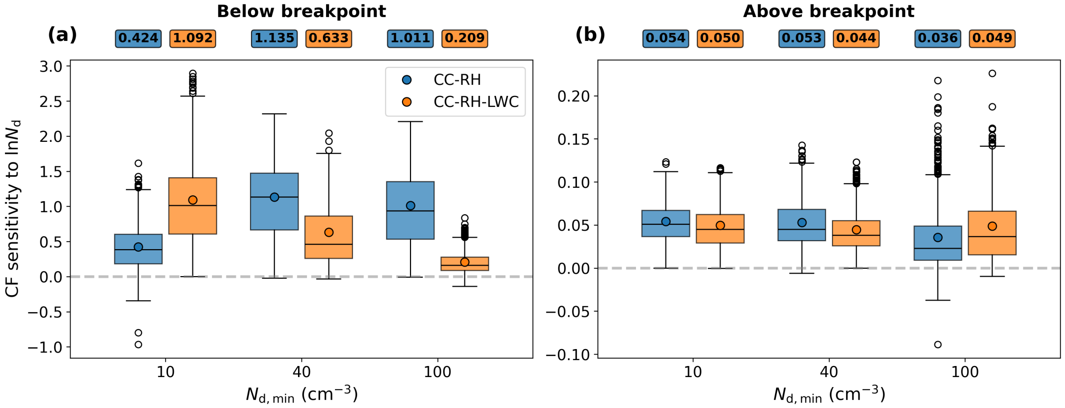

Figure 5. Global distributions of the cloud fraction sensitivity to log-transformed cloud droplet number concentration ($\ln N_{\mathrm{d}}$) for global marine liquid clouds during 2011–2015, for six experiments (two cloud cover parameterization schemes: CC-RH and CC-RH-LWC; three imposed N_{d} lower bounds $N_{\mathrm{d,min}}$ = 10, 40 and 100 cm^{-3}). Sensitivities are computed within each $5^{\circ} \times 5^{\circ}$ oceanic window using a piecewise linear regression between $\ln N_{\mathrm{d}}$ feature values and $\ln N_{\mathrm{d}}$ SHAP values, with a single breakpoint $\ln(N_{\mathrm{d,bp}}) = \ln(\mathrm{N_{d,min}}) + 0.1$. (a) below-breakpoint sensitivities; (b) above-breakpoint sensitivities; Box plots display the interquartile range (IQR), whiskers extend to 1.5 × IQR, and circles denote outliers; medians are horizontal lines. Area-weighted means are shown as circular markers with connecting lines, and the floating values above each panel denote the corresponding area-weighted mean sensitivities. Note that the y-axis ranges differ between panels.

PLR approach is not merely an ad hoc curve-fitting choice but effectively captures the model's physical transition from a highly sensitive, aerosol-limited regime to a saturated regime. Moreover, the consistent breakpoint range reinforces that our central findings—the headroom-mediated sensitivity patterns and the counterintuitive CC-RH > CC-RH-LWC sensitivity contrast at high $N_{\mathrm{d,min}}$—are robust and reflect genuine ICON-HAM's simulated physics.

3.4 Implications for the forcing estimate

3.4.1 For the bottom-up approach (GCM PI–PD paired simulations)

Our findings reveal a potential challenge in quantifying the radiative forcing from the CF adjustment, as the detected sensitivity is highly state-dependent. Our findings have different implications for different methods to estimate forcing: the bottom-up approach (GCM PI–PD paired simulations) and the top-down approach (observational sensitivity-based).

GCMs typically estimate effective radiative forcing due to ACI using a bottom-up method by running paired PI and PD simulations and taking their difference in the net radiation at the TOA (Ghan, 2013; Boucher et al., 2013; Smith et al., 2020), without relying on an explicit sensitivity value. Instead, the aerosol-cloud forcing emerges from the full nonlinear response across the PI–PD aerosol contrast. Our analysis, in contrast, focuses on the local PD-state $\ln N_{\mathrm{d}}$–CF sensitivity across six ICON-HAM experiments. These PD-state slopes are therefore not a direct measure of CF-adjustment forcing, but they describe how

© Author(s) 2026. CC BY 4.0 License.

efficiently additional N_d changes can still modify CF once the system has already reached its PD baseline. Here, we discuss how our findings from these different ICON-HAM configurations potentially affect aerosol forcing estimates.

As systematically investigated by Hoose et al. (2009), imposing $N_\mathrm{d,min}$ unphysically alters both the PI and PD states, creating artificially polluted PI conditions over both land and ocean and artificially polluted PD conditions over oceans. This makes the contrast between PI and PD collapse and strongly damps the total aerosol indirect effects. Our experiments add a previously undocumented, complementary dimension to this result by introducing the CC-RH-LWC scheme. When this scheme is combined with high $N_\mathrm{d,min}$, suppressed autoconversion raises LWP and thereby elevates baseline CF in both PI and PD equilibrium states. Under naturally pristine PI conditions, this combination can already pre-saturates clouds. In the PD state, anthropogenic aerosols increases cannot further increase CF because clouds already operate near the CF ≈ 1 ceiling. In addition to the $N_\mathrm{d,min}$-alone effect (reduced PI–PD N_d contrast) on the total forcing owing to ACI identified by Hoose et al. (2009), this bilateral saturation through the headroom effect compresses the PI–PD ΔCF and physically suppresses the CF-adjustment component of the forcing. For the CC-RH scheme, which lacks the direct LWC-CF link, baseline CF does not saturate to the same extent (Fig. 1c), so the forcing is mainly altered by $N_\mathrm{d,min}$ alone as in Hoose et al. (2009).

On the other hand, our study also adds a new angle to Lohmann and Feichter (1997). Their work compared an LWC-dependent and an RH-only cloud-cover scheme (referred to as COUPL-CC and COUPL, respectively) and their resulting PI–PD changes in CF and the total aerosol indirect effect, but without imposing $N_\mathrm{d,min}$. $N_\mathrm{d,min}$ was only introduced in ECHAM4 later by Lohmann et al. (1999). Without $N_\mathrm{d,min}$, there is no associated increase in baseline CF and thus PI clouds are not pre-saturated. Consequently, there is sufficient headroom and anthropogenic aerosols can increase CF without being immediately constrained by the CF ceiling in either COUPL or COUPL-CC. Therefore, the stronger dependence on cloud water in COUPL-CC produces larger CF increases and a more negative total indirect effect than the RH-only COUPL scheme. This behaviour is qualitatively consistent with our ICON-HAM experiments at a low $N_\mathrm{d,min}$ of $10\ \mathrm{cm}^{-3}$, where CC-RH-LWC shows a larger marginal contribution of $\ln N_\mathrm{d}$ (Fig. 4b) and a stronger $\ln N_\mathrm{d}$–CF PD-state sensitivity (Fig. 5a) than CC-RH. In both studies, a cloud-water–dependent scheme responds more strongly than an RH-only scheme when $N_\mathrm{d,min}$ is effectively low. However, at higher $N_\mathrm{d,min}$, the ordering reverses (i.e. CC-RH becomes stronger) due to the headroom effect. Extrapolating this behaviour to the Lohmann and Feichter (1997) framework, one would expect that imposing a high $N_\mathrm{d,min}$ in their COUPL versus COUPL-CC comparison would reduce the PI–PD CF increase in both schemes and thereby shrink the difference in total aerosol indirect effect between them. A complete reversal in the forcing order, analogous to the reversal seen in our $\ln N_\mathrm{d}$–CF sensitivities at high $N_\mathrm{d,min}$, seems less likely. Lohmann and Feichter (1997) quantified the ACI forcing from PI to PD including non-CF components, whereas the headroom effect identified here acts specifically on the CF-adjustment component and is inferred from PD-state sensitivity variability rather than from an explicit PI–PD forcing calculation.

Overall, if CC-RH-LWC is used, this strong reduction in the CF-adjustment forcing is already operative at $N_\mathrm{d,min} = 40\ \mathrm{cm}^{-3}$, which is the default value in the ECHAM and ICON model families. Although we do not perform explicit PI–PD runs or compute the radiative forcing from CF adjustments, it is reasonable to expect that the combination of a CC-RH-LWC–type parameterization with high $N_\mathrm{d,min}$ would weaken the CF-adjustment contribution to effective radiative forcing from ACI in a bottom-up setup, especially over clean oceanic regions. This tendency would further widen the gap between model-based estimates that attribute only a minor role to CF adjustment (e.g. Smith et al., 2020; Zelinka et al., 2023) and observation-based studies that identify CF adjustment as a primary component (e.g. Chen et al., 2022; Wall et al., 2023; Yuan et al., 2023). These implications remain qualitative, as they are inferred from PD-state sensitivities rather than aerosol forcing diagnostics; a natural next step is to repeat our ICON-HAM experiments for paired PI–PD simulations and explicitly diagnose the CF-adjustment contribution to the aerosol-cloud forcing to test this hypothesis.

3.4.2 For the top-down approach (observational sensitivity-based)

In contrast to the bottom-up PI–PD approach, observational studies often follow a top-down strategy, in which CF-adjustment forcing is inferred from an explicit sensitivity value. These strategies vary: some exploit localized perturbations to isolate aerosol effects by deriving N_d–CF sensitivities from contrasts between relatively clean background conditions and nearby polluted perturbations (e.g. ship tracks or volcanic events) and directly calculate the radiative effect of the associated CF adjustments (e.g. Chen et al., 2022; Yuan et al., 2023), while others diagnose aerosol–CF sensitivities from statistical relationships across PD variability and apply cloud radiative kernels to the derived cloud-property changes (e.g. Wall et al., 2023). In all of these frameworks, the inferred sensitivity in the sampled cloud regimes is central, as it links observed variability to radiative forcing.

Our results highlight that such sensitivities are strongly state-dependent. In ICON-HAM, the headroom effect appears most clearly when high $N_\mathrm{d,min}$ is combined with CC-RH-LWC, which pushes baseline CF close to its saturation limit and suppresses the PD-state $\ln N_\mathrm{d}$–CF sensitivity. Part of this pre-saturation is clearly structural to climate models, arising from the imposed $N_\mathrm{d,min}$ and the chosen cloud-cover formulation. In the real atmosphere, there is neither $N_\mathrm{d,min}$ nor a prescribed scheme, but there is still physical saturation of CF in regimes with high LWP or RH. Any observationally derived N_d–CF slope will therefore reflect the headroom available in the sampled clouds: sensitivities diagnosed in already cloudy, high-LWP regimes will tend to be weaker than those in thinner, less saturated regimes. This aligns with previous findings that N_d–CF sensitivities are strongest near the edges of the stratocumulus field and in stratocumulus-to-cumulus transition regions, rather than within the overcast decks (Gryspeerdt et al., 2016; Jia et al., 2024).

This state-dependence has implications for interpreting observational constraints on CF-adjustment forcing. Most recent observation-based estimates (e.g. Chen et al., 2022; Wall et al., 2023; Yuan et al., 2023; Chen et al., 2024) use natural experiments or from PD aerosol–cloud relationships, which do not require assuming a single fixed N_d –CF sensitivity that can be applied to infer changes from PI to PD. However, the underlying N_d–CF relationships in these studies are still diagnosed from specific cloud regimes in the current climate, where baseline CF varies and thus the remaining potential for CF to increase differs. Consequently, the inferred sensitivities are conditional on the mean state and may not be directly transferable to a PI–PD forcing context, since sensitivities in already-cloudy, low-headroom regimes could underestimate the potential response in cleaner, less saturated conditions (representative of PI). A more complete understanding of the CF adjustment to the aerosol forcing would therefore benefit from explicitly conditioning sensitivities on baseline cloud state (e.g. CF, LWP, and precipitation regime) as a complement to regime-aggregated estimates. This is particularly relevant given the likely reduction in MLC cover in a warming world (Myers et al., 2021; Forster et al., 2021; Bock and Lauer, 2024), which would increase the available headroom and thus potentially enhance the CF sensitivity. This would facilitate more consistent comparisons between model-based and observational estimates by accounting for how the available headroom for CF increases varies systematically across different cloud states.

4 Conclusions

This study extends the explainable ML framework from our previous observational study (J24) to the ICON-HAM atmosphere-aerosol model. Our primary goals were to compare MODIS- and ICON-HAM-based $\ln N_\mathrm{d}$–CF sensitivities in MLCs, and to understand how the cloud-cover schemes and $N_\mathrm{d,min}$ jointly shape the simulated CF response. To achieve this, we conducted six experiments, which are combined with two cloud-cover schemes, one dependent solely on relative humidity (CC-RH) and one additionally dependent on cloud water content (CC-RH-LWC), and three different $N_\mathrm{d,min}$ = 10, 40, and 100 cm^{-3}. The findings of our study are summarized as follows:

1. Mean-state response to $N_\mathrm{d,min}$ and cloud-cover schemes: Higher $N_\mathrm{d,min}$ suppresses autoconversion and drizzle, and builds up liquid water in both schemes. The CC-RH-LWC scheme translates this LWP increase directly into elevated CF due to its explicit cloud-water dependence, whereas CC-RH, lacking this direct link, shows a weaker or even declining CF response. At $N_\mathrm{d,min}$ = 40 and 100 cm^{-3}, this creates markedly different mean background cloud conditions between the schemes.
2. ICON-HAM simulates a non-linearity in the $\ln N_\mathrm{d}$–CF relationship: The ICON-HAM $\ln N_\mathrm{d}$–CF relationship is strongly non-linear and shows a clear saturation effect that persists even after log-transformation. This contrasts with the observation-based relationship, which has been shown to be linear in logarithmic space. The difference likely reflects ICON-HAM's process-level parameterizations that retain small-scale saturation effects from field campaigns or LES studies, whereas satellite observations at larger scales show smoother responses due to spatial averaging.
3. Headroom-mediated $\ln N_\mathrm{d}$–CF sensitivity: The mean-state physics in point 1 sets the baseline CF in ICON-HAM. The SHAP approach reveals that high SHAP base values (baseline CF) limit the marginal contribution of $\ln N_\mathrm{d}$ (Fig. 4), leading to weaker detected sensitivity (Fig. 5), despite the direct physical coupling between CF and cloud water, creating a headroom effect. At $N_\mathrm{d,min}$ = 10 cm^{-3}, CC-RH-LWC is more sensitive to $\ln N_\mathrm{d}$ due to its direct dependence on LWC. This pattern reverses at $N_\mathrm{d,min}$ = 40 and 100 cm^{-3}, as high $N_\mathrm{d,min}$ together with CC-RH-LWC leaves little headroom, while CC-RH preserves a lower baseline CF and thus more room for $\ln N_\mathrm{d}$-driven changes.
4. Methodological extension and breakpoint robustness: Three breakpoint strategies consistently separate a steep low-N_d regime and a flatter high-N_d regime, and the contrasting patterns are qualitatively consistent across all experiments. For ICON-HAM's default $N_\mathrm{d,min}$ = 40 cm^{-3}, the statistically optimized breakpoints converge at approximately 50–60 cm^{-3}, consistent with observed N_d–CF saturation thresholds, supporting the robustness of our framework. More importantly, this suggests that the default $N_\mathrm{d,min}$ setup provides a physically consistent representation of the transition into the saturation regime.

5. Implications for CF adjustment forcing and model–observation comparisons: For GCMs using bottom-up PI–PD methods, high $N_{\mathrm{d,min}}$ values combined with LWC-dependent cloud-cover schemes can pre-saturate both PI and PD cloud fields, damping CF adjustment forcing even when the underlying model physics is strong. In top-down, observation-based approaches, any diagnosed N_{d}–CF sensitivity is inherently state-dependent and reflects the available headroom in the sampled cloud regimes. This implies that robust CF adjustment constraints should explore the option to condition sensitivities on baseline cloud state (e.g. CF, LWP, and precipitation regime), rather than treating the N_{d}–CF sensitivity as a single, regime-independent quantity.

Code availability. Code is available from the corresponding author upon reasonable request.

Data availability. All model output analyzed in this study was generated using ICON-HAM version 2.6.4. Due to the large data volume, the model output is not publicly archived but is available from the corresponding author upon reasonable request. The MODIS satellite observations and reanalysis data used for comparison in Fig. 2a and Fig. S2a were obtained from the sources described in Jia et al. (2024).

Appendix A: Predictor variables

Appendix B: Piecewise SHAP sensitivity with two alternative breakpoint strategies

B1 Constraint-aware breakpoint with fixed interval in linear space

To assess how the choice of breakpoints influences our results, we introduce two additional breakpoint strategies. The first one is likewise constraint-aware, as the breakpoint is defined relative to $N_{\mathrm{d,min}}$. However, the interval is specified in linear rather than logarithmic space:

$$\ln(N_{\mathrm{d,bp}}) = \ln(\mathrm{N_{d,min}} + \Delta N_{\mathrm{d}}) \tag{B1}$$

where $N_{\mathrm{d,bp}}$ denotes the breakpoint and ΔN_{d} represents the offset in linear space (in cm^{-3}) from the imposed lower bound. For this test, we set $\Delta N_{\mathrm{d}} = 5\ \mathrm{cm}^{-3}$, yielding breakpoints of 15, 45 and 105 cm^{-3} for $N_{\mathrm{d,min}}$ = 10, 40, and 100 cm^{-3}, respectively.

On the logarithmic scale, the interval between $N_{\mathrm{d,min}}$ and the breakpoint equals $\ln(1+\frac{\Delta N_{\mathrm{d}}}{\mathrm{N_{d,min}}})$, which shrinks as $N_{\mathrm{d,min}}$ increases. The log-space interval width is $\ln(1.5)$, $\ln(1.125)$, $\ln(1.05)$ for $N_{\mathrm{d,min}}$ = 10, 40 and 100 cm^{-3}, respectively. Thus, as $N_{\mathrm{d,min}}$ increases, the prescribed truncation becomes tighter and causes more data points to pile up near $N_{\mathrm{d,min}}$. This already increases the y-axis (SHAP value) spread within a narrow x-axis range. The shrinking intervals further compress the near-$N_{\mathrm{d,min}}$ regime on the x-axis while the associated SHAP response variability on the y-axis remains comparatively strong, leading to an inflated β_b at higher $N_{\mathrm{d,min}}$ values.

© Author(s) 2026. CC BY 4.0 License.

Table A1. Overview of the predictors from ICON-HAM. Numeric subscripts denote pressure levels or altitudes.

Predictor variable	**Short name**	**Unit**
Relative humidity	RH_{700}, RH_{850}, RH_{900}, RH_{950}	%
Specific humidity	SH_{700}, SH_{850}	$\mathrm{kg\,kg^{-1}}$
Air temperature	t_{700}, t_{850}	K
Vertical velocity	ω_{700}, ω_{850}	$\mathrm{Pa\,s^{-1}}$
Zonal (eastward) wind	u_{700}, u_{850}	$\mathrm{m\,s^{-1}}$
Meridional (northward) wind	v_{700}, v_{850}	$\mathrm{m\,s^{-1}}$
Eastward and northward wind component at 10 m	u_{10}, v_{10}	$\mathrm{m\,s^{-1}}$
Boundary-layer height (proxy)	BLH	m
Sea surface temperature	SST	K
Vertically integrated water vapour	VIWV	$\mathrm{kg\,m^{-2}}$
Large-scale precipitation flux (water)	PR	$\mathrm{kg\,m^{-2}\,s^{-1}}$
Sensible heat flux	SHF	$\mathrm{W\,m^{-2}}$
Latent heat flux	LHF	$\mathrm{W\,m^{-2}}$
Estimated inversion strength (calculated)	EIS	K
Natural logarithm of cloud droplet number concentration	$\ln N_\mathrm{d}$	dimensionless (N_d in $\mathrm{cm^{-3}}$)

This inflated β_b is visible both in Figs. B1 and B2 for the CC-RH parameterization as $N_\mathrm{d,min}$ increases. It does not occur for CC-RH-LWC because the compression effect is outweighed by the headroom limitation. Despite these quantitative differences in the slopes, the main qualitative conclusions remain robust: First, below-breakpoint $\ln N_\mathrm{d}$–CF sensitivities are larger than those above the breakpoint regime, and inter-experiment contrasts are only evident in the below-breakpoint regime. Second, at $N_\mathrm{d,min}$ = 10 $\mathrm{cm^{-3}}$, CC-RH-LWC has stronger sensitivities owing to its direct dependence on cloud water content; at $N_\mathrm{d,min}$ = 40 and 100 $\mathrm{cm^{-3}}$, CC-RH shows stronger sensitivities because of the headroom effect arising from CC-RH-LWC's elevated baseline CF and a CF = 1.0 cap. Choosing this breakpoint strategy primarily affects the trend of sensitivity with increasing $N_\mathrm{d,min}$ within each cloud-cover regime. The extent to which this x-range compression influences the results depends on its relative strength versus the headroom effect.

B2 Statistically optimized constraint-aware breakpoint

To further evaluate the robustness of our results, we apply a statistically optimized strategy. This data-driven approach determines breakpoints by optimizing their locations that minimize the overall sum of squared errors of the two-segment PLR fit, but constrains the search range to [ln($N_\mathrm{d,min}$), ln($N_\mathrm{d,min}$ + 50)]. This hybrid design is therefore constraint-aware while allowing the data to determine the exact split location.

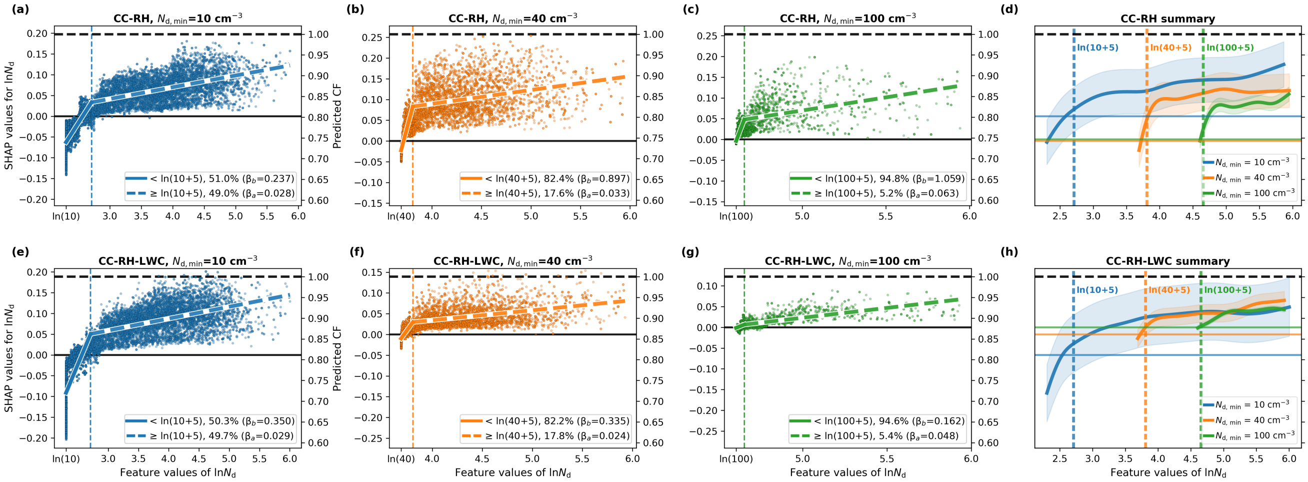

Figure B1. As in Fig. 3, but the breakpoint for the piecewise linear regression is defined as $\ln(N_{\mathrm{d,bp}}) = \ln(\mathrm{N}_{\mathrm{d,min}} + 5)$.

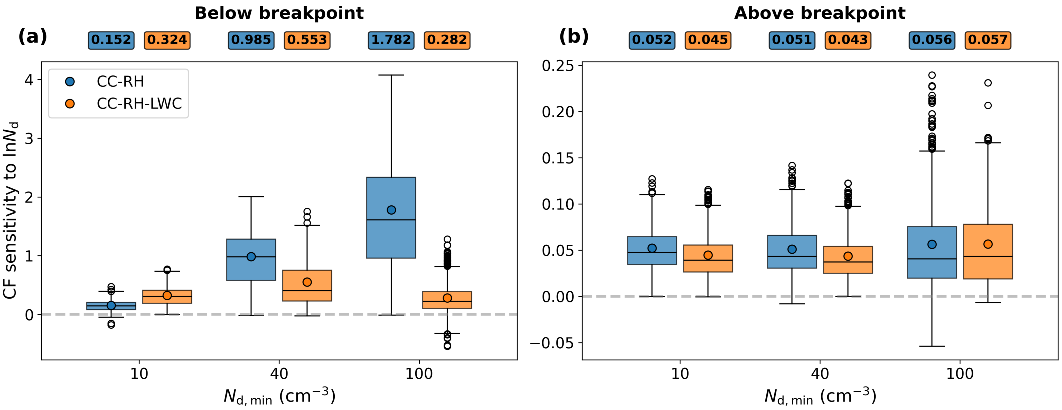

Figure B2. Similar to Fig. 5, except the breakpoint for the piecewise linear regression is defined as $\ln(N_{\mathrm{d,bp}}) = \ln(\mathrm{N}_{\mathrm{d,min}} + 5)$.

To ensure statistical robustness, this hybrid strategy enforces per-regime sample minima of 1000 data points below the breakpoint and 500 above. These thresholds serve two purposes: first, a pre-fit feasibility check verifies whether any breakpoint within the bounded range can satisfy both minima at the same time, triggering the fallback if no feasible split exists; second, a post-fit validation checks the actual final regime sizes, setting slopes to NaN if either regime is insufficient. Additionally, we set a fit quality screen accepting the piecewise fit only if $R^2 \geq 0.70$ and root mean square error (RMSE) improves by at least 5 % compared to a single linear regression. If either the quality criteria fail, or no feasible split exists within the bounded range, we fall back to $\ln(N_{\mathrm{d,bp}}) = \ln(\mathrm{N}_{\mathrm{d,min}}) + 0.1$. Per-regime sample minima are enforced at the slope-estimation stage; if only one regime lacks sufficient samples, that slope is set to NaN (no fallback), whereas a complete failure (both slopes invalid) triggers

https://doi.org/10.5194/egusphere-2026-569
Preprint. Discussion started: 20 February 2026
© Author(s) 2026. CC BY 4.0 License.

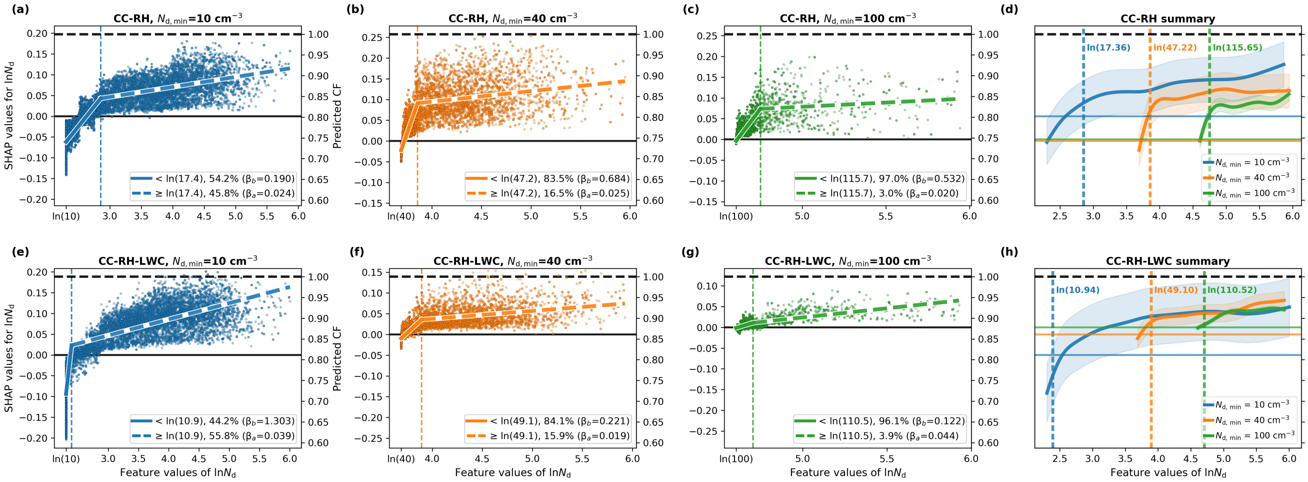

Figure B3. Similar to Fig. 3, except the breakpoints for the piecewise linear regression are statistically optimized.

the fallback. Finally, we apply an interquartile-range-based outlier filter (with a multiplier of 2.0) and a slope-consistency check to remove unphysical or outlying slope estimates.

This hybrid strategy yields Fig. B3 and Fig. B4. Again, both from the exemplary geographical window perspective and the global perspective, the key pattern persists. Particularly in the below-breakpoint regime, CC-RH-LWC shows stronger sensitivity at $N_{\mathrm{d,min}} = 10\ \mathrm{cm}^{-3}$ through its cloud water dependence, while CC-RH is stronger at 40 and 100 cm^{-3} due to headroom constraints in CC-RH-LWC. Overall, the inter-$N_{\mathrm{d,min}}$ and inter-scheme contrasts obtained with this data-driven strategy (Fig. B4) are consistent with those from the constraint-aware approach with a fixed interval in log space (Fig. 5), confirming that our key scientific conclusions are robust to the choice of breakpoint strategy.

We additionally show the global distribution of the optimized breakpoints using this strategy in Fig. B4c. For the default ICON-HAM configuration ($N_{\mathrm{d,min}} = 40\ \mathrm{cm}^{-3}$), the area-weighted global mean optimized breakpoints are approximately 48 and 56 cm^{-3} on a linear scale for CC-RH and CC-RH-LWC, respectively. These values align closely with the observational saturation thresholds discussed in the main text (Sect. 3.3.4), providing physical support for the statistically optimized breakpoint locations (see main text for detailed discussion).

Author contributions. YJ, HA, JC, DN and UL designed the study. YJ, HA, DN, and UL developed the methodology. DN developed the ICON-HAM model configuration. YJ performed the model simulations, implemented the machine learning framework, analyzed the data, and created the visualizations. HA contributed extensively to the data analysis and interpretation throughout the study. UL, DN, and CH provided specific scientific insights regarding model configuration and the interpretation of findings. YJ wrote the original draft, and all authors reviewed and improved the manuscript.

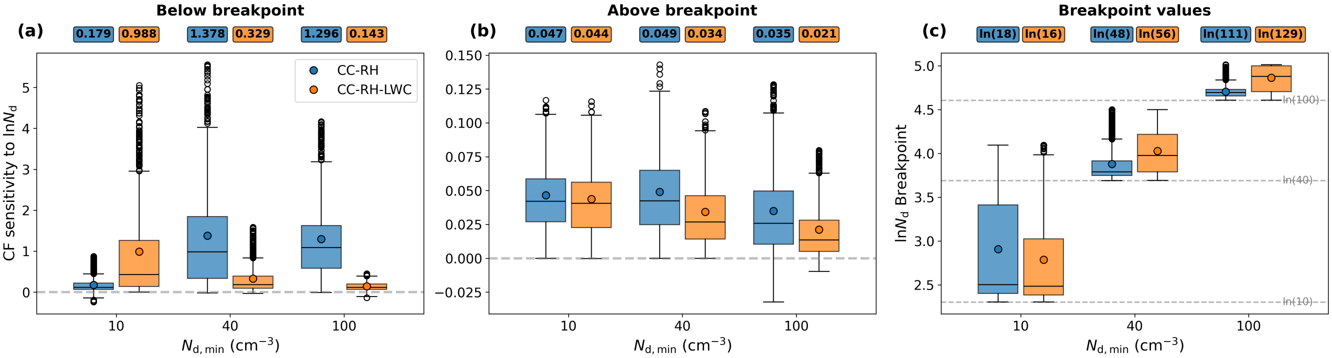

Figure B4. As in Fig. 5, but the breakpoints for the piecewise linear regression are statistically optimized (their distributions are shown in panel (c)).

Competing interests. The contact author has declared that none of the authors has any competing interests.

Acknowledgements. The first author acknowledges funding from the European Union's Horizon 2020 research and innovation programme under grant agreement no. 821205 (FORCeS) and the Deutsche Forschungsgemeinschaft (DFG) in the project Constraining Aerosol-Low cloud InteractionS with multi-target MAchine learning (CALISMA), project number 440521482. The first author also gratefully acknowledges the Graduate School for Climate and Environment (GRACE) at KIT for funding a research visit to ETH Zurich that enabled this collaboration. Generative AI tools were used to help brainstorm, structural refinement and language polishing, but no large blocks of text were directly generated by AI. All authors have reviewed all changes and assume full responsibility for the content.

© Author(s) 2026. CC BY 4.0 License.

References

Ackerman, A. S., Kirkpatrick, M. P., Stevens, D. E., and Toon, O. B.: The impact of humidity above stratiform clouds on indirect aerosol climate forcing, Nature, 432, 1014–1017, https://doi.org/10.1038/nature03174, 2004.

Albrecht, B. A.: Aerosols, cloud microphysics, and fractional cloudiness, Science, 245, 1227–1230, https://doi.org/10.1126/science.245.4923.1227, 1989.

Andersen, H., Cermak, J., Fuchs, J., Knutti, R., and Lohmann, U.: Understanding the drivers of marine liquid-water cloud occurrence and properties with global observations using neural networks, Atmospheric Chemistry and Physics, 17, 9535–9546, https://doi.org/10.5194/acp-17-9535-2017, 2017.

Andersen, H., Cermak, J., Douglas, A., Myers, T. A., Nowack, P., Stier, P., Wall, C. J., and Wilson Kemsley, S.: Sensitivities of cloud radiative effects to large-scale meteorology and aerosols from global observations, Atmospheric Chemistry and Physics, 23, 10 775–10 794, https://doi.org/10.5194/acp-23-10775-2023, 2023.

Bellouin, N., Quaas, J., Gryspeerdt, E., Kinne, S., Stier, P., Watson-Parris, D., Boucher, O., Carslaw, K. S., Christensen, M., Daniau, A. L., Dufresne, J. L., Feingold, G., Fiedler, S., Forster, P., Gettelman, A., Haywood, J. M., Lohmann, U., Malavelle, F., Mauritsen, T., McCoy, D. T., Myhre, G., Mülmenstädt, J., Neubauer, D., Possner, A., Rugenstein, M., Sato, Y., Schulz, M., Schwartz, S. E., Sourdeval, O., Storelvmo, T., Toll, V., Winker, D., and Stevens, B.: Bounding Global Aerosol Radiative Forcing of Climate Change, Reviews of Geophysics, 58, 1–45, https://doi.org/10.1029/2019RG000660, 2020.

Bender, F. A., Frey, L., McCoy, D. T., Grosvenor, D. P., and Mohrmann, J. K.: Assessment of aerosol–cloud–radiation correlations in satellite observations, climate models and reanalysis, Climate Dynamics, 52, 4371–4392, https://doi.org/10.1007/s00382-018-4384-z, 2019.

Bock, L. and Lauer, A.: Cloud properties and their projected changes in CMIP models with low to high climate sensitivity, Atmospheric Chemistry and Physics, 24, 1587–1605, https://doi.org/10.5194/acp-24-1587-2024, 2024.

Boucher, O., Granier, C., Hoose, C., and Andy, J.: Clouds and aerosols, Climate Change 2013 the Physical Science Basis: Working Group I Contribution to the Fifth Assessment Report of the Intergovernmental Panel on Climate Change, 9781107057, 571–658, https://doi.org/10.1017/CBO9781107415324.016, 2013.

Bretherton, C. S., Blossey, P. N., and Uchida, J.: Cloud droplet sedimentation, entrainment efficiency, and subtropical stratocumulus albedo, Geophysical Research Letters, 34, https://doi.org/https://doi.org/10.1029/2006GL027648, 2007.

Bretherton, C. S., Blossey, P. N., and Jones, C. R.: Mechanisms of marine low cloud sensitivity to idealized climate perturbations: A single-LES exploration extending the CGILS cases, Journal of Advances in Modeling Earth Systems, 5, 316–337, https://doi.org/https://doi.org/10.1002/jame.20019, 2013.

Chen, T. and Guestrin, C.: XGBoost: A Scalable Tree Boosting System, in: Proceedings of the 22nd ACM SIGKDD International Conference on Knowledge Discovery and Data Mining, KDD '16, pp. 785–794, ACM, https://doi.org/10.1145/2939672.2939785, 2016.

Chen, Y., Haywood, J., Wang, Y., Malavelle, F., Jordan, G., Partridge, D., Fieldsend, J., De Leeuw, J., Schmidt, A., Cho, N., Oreopoulos, L., Platnick, S., Grosvenor, D., Field, P., and Lohmann, U.: Machine learning reveals climate forcing from aerosols is dominated by increased cloud cover, Nature Geoscience, 15, 609–614, https://doi.org/10.1038/s41561-022-00991-6, 2022.

Chen, Y., Haywood, J., Wang, Y., Malavelle, F., Jordan, G., Peace, A., Partridge, D. G., Cho, N., Oreopoulos, L., Grosvenor, D., Field, P., Allan, R. P., and Lohmann, U.: Substantial cooling effect from aerosol-induced increase in tropical marine cloud cover, Nature Geoscience, https://doi.org/10.1038/s41561-024-01427-z, 2024.

Chen, Y. C., Christensen, M. W., Stephens, G. L., and Seinfeld, J. H.: Satellite-based estimate of global aerosol-cloud radiative forcing by marine warm clouds, Nature Geoscience, 7, 643–646, https://doi.org/10.1038/ngeo2214, 2014.

Christensen, M. W., Jones, W. K., and Stier, P.: Aerosols enhance cloud lifetime and brightness along the stratus-to-cumulus transition, Proceedings of the National Academy of Sciences of the United States of America, 117, 17 591–17 598, https://doi.org/10.1073/pnas.1921231117, 2020.

Duran, B. M., Wall, C. J., Lutsko, N. J., Michibata, T., Ma, P.-L., Qin, Y., Duffy, M. L., Medeiros, B., and Debolskiy, M.: A new method for diagnosing effective radiative forcing from aerosol–cloud interactions in climate models, Atmospheric Chemistry and Physics, 25, 2123–2146, https://doi.org/10.5194/acp-25-2123-2025, 2025.

Fons, E., Naumann, A. K., Neubauer, D., Lang, T., and Lohmann, U.: Investigating the sign of stratocumulus adjustments to aerosols in the ICON global storm-resolving model, Atmospheric Chemistry and Physics, 24, 8653–8675, https://doi.org/10.5194/acp-24-8653-2024, 2024.

Forster, P. M., Storelvmo, T., Armour, K., Collins, W., Dufresne, J. L., Frame, D., Lunt, D. J., Mauritsen, T., Palmer, M. D., Watanabe, M., Wild, M., and Zhang, H.: Chapter 7: The Earth's Energy Budget, Climate Feedbacks, and Climate Sensitivity, in: Climate Change 2021: The Physical Science Basis. Contribution of Working Group I to the Sixth Assessment Report of the Intergovernmental Panel on Climate Change, edited by Masson-Delmotte, V., Zhai, P., Pirani, A., Connors, S. L., Péan, C., Berger, S., Caud, N., Chen, Y., Goldfarb, L., Gomis, M. I., Huang, M., Leitzell, K., Lonnoy, E., Matthews, J., Maycock, T. K., Waterfield, T., Yelekçi, O., Yu, R., and Zhou, B., p. in press, Cambridge University Press, 2021.

Franke, H. and Giorgetta, M. A.: Toward the Direct Simulation of the Quasi-Biennial Oscillation in a Global Storm-Resolving Model, Journal of Advances in Modeling Earth Systems, 16, e2024MS004 381, https://doi.org/https://doi.org/10.1029/2024MS004381, 2024.

Fuchs, J., Cermak, J., and Andersen, H.: Building a cloud in the southeast Atlantic: Understanding low-cloud controls based on satellite observations with machine learning, Atmospheric Chemistry and Physics, 18, 16 537–16 552, https://doi.org/10.5194/acp-18-16537-2018, 2018.

Ghan, S. J.: Technical note: Estimating aerosol effects on cloud radiative forcing, Atmospheric Chemistry and Physics, 13, 9971–9974, https://doi.org/10.5194/acp-13-9971-2013, 2013.

Giorgetta, M. A., Brokopf, R., Crueger, T., Esch, M., Fiedler, S., Helmert, J., Hohenegger, C., Kornblueh, L., Köhler, M., Manzini, E., Mauritsen, T., Nam, C., Raddatz, T., Rast, S., Reinert, D., Sakradzija, M., Schmidt, H., Schneck, R., Schnur, R., Silvers, L., Wan, H., Zängl, G., and Stevens, B.: ICON-A, the Atmosphere Component of the ICON Earth System Model: I. Model Description, Journal of Advances in Modeling Earth Systems, 10, 1613–1637, https://doi.org/https://doi.org/10.1029/2017MS001242, 2018.

Giorgetta, M. A., Sawyer, W., Lapillonne, X., Adamidis, P., Alexeev, D., Clément, V., Dietlicher, R., Engels, J. F., Esch, M., Franke, H., Frauen, C., Hannah, W. M., Hillman, B. R., Kornblueh, L., Marti, P., Norman, M. R., Pincus, R., Rast, S., Reinert, D., Schnur, R., Schulzweida, U., and Stevens, B.: The ICON-A model for direct QBO simulations on GPUs (version icon-cscs:baf28a514), Geoscientific Model Development, 15, 6985–7016, https://doi.org/10.5194/gmd-15-6985-2022, 2022.

Goren, T., Kazil, J., Hoffmann, F., Yamaguchi, T., and Feingold, G.: Anthropogenic Air Pollution Delays Marine Stratocumulus Breakup to Open Cells, Geophysical Research Letters, 46, 14 135–14 144, https://doi.org/https://doi.org/10.1029/2019GL085412, 2019.

Goren, T., Feingold, G., Gryspeerdt, E., Kazil, J., Kretzschmar, J., Jia, H., and Quaas, J.: Projecting Stratocumulus Transitions on the Albedo—Cloud Fraction Relationship Reveals Linearity of Albedo to Droplet Concentrations, Geophysical Research Letters, 49, e2022GL101 169, https://doi.org/https://doi.org/10.1029/2022GL101169, 2022.

Gryspeerdt, E., Quaas, J., and Bellouin, N.: Constraining the aerosol influence on cloud fraction, Journal of Geophysical Research, 121, 3566–3583, https://doi.org/10.1002/2015JD023744, 2016.

Gryspeerdt, E., Goren, T., Sourdeval, O., Quaas, J., Mülmenstädt, J., Dipu, S., Unglaub, C., Gettelman, A., and Christensen, M.: Constraining the aerosol influence on cloud liquid water path, Atmospheric Chemistry and Physics, 19, 5331–5347, https://doi.org/10.5194/acp-19-5331-2019, 2019.

Gryspeerdt, E., Mülmenstädt, J., Gettelman, A., Malavelle, F. F., Morrison, H., Neubauer, D., Partridge, D. G., Stier, P., Takemura, T., Wang, H., Wang, M., and Zhang, K.: Surprising similarities in model and observational aerosol radiative forcing estimates, Atmospheric Chemistry and Physics, 20, 613–623, https://doi.org/10.5194/acp-20-613-2020, 2020.

Hartmann, D. L., Ockert-Bell, M. E., and Michelsen, M. L.: The Effect of Cloud Type on Earth's Energy Balance: Global Analysis, Journal of Climate, 5, 1281–1304, https://doi.org/10.1175/1520-0442(1992)005<1281:TEOCTO>2.0.CO;2, 1992.

Held, I. M. and Soden, B. J.: Robust Responses of the Hydrological Cycle to Global Warming, Journal of Climate, 19, 5686–5699, https://doi.org/https://doi.org/10.1175/JCLI3990.1, 2006.

Hoose, C., Kristjánsson, J. E., Iversen, T., Kirkevåg, A., Seland, Ø., and Gettelman, A.: Constraining cloud droplet number concentration in GCMs suppresses the aerosol indirect effect, Geophysical Research Letters, 36, https://doi.org/https://doi.org/10.1029/2009GL038568, 2009.

Hu, S., Zhu, Y., Rosenfeld, D., Mao, F., Lu, X., Pan, Z., Zang, L., and Gong, W.: The Dependence of Ship-Polluted Marine Cloud Properties and Radiative Forcing on Background Drop Concentrations, Journal of Geophysical Research: Atmospheres, 126, e2020JD033 852, https://doi.org/https://doi.org/10.1029/2020JD033852, 2021.

Jia, Y., Andersen, H., and Cermak, J.: Analysis of the cloud fraction adjustment to aerosols and its dependence on meteorological controls using explainable machine learning, Atmospheric Chemistry and Physics, 24, 13 025–13 045, https://doi.org/10.5194/acp-24-13025-2024, 2024.

Khairoutdinov, M. and Kogan, Y.: A New Cloud Physics Parameterization in a Large-Eddy Simulation Model of Marine Stratocumulus, Monthly Weather Review, 128, 229–243, https://doi.org/https://doi.org/10.1175/1520-0493(2000)128<0229:ANCPPI>2.0.CO;2, 2000.

Kirkevåg, A., Iversen, T., Seland, Ø., Debernard, J. B., Storelvmo, T., and Kristjánsson, J. E.: Aerosol-cloud-climate interactions in the climate model CAM-Oslo, Tellus A: Dynamic Meteorology and Oceanography, 60, 492, https://doi.org/10.1111/j.1600-0870.2007.00313.x, 2008.

Leahy, L. V., Wood, R., Charlson, R. J., Hostetler, C. A., Rogers, R. R., Vaughan, M. A., and Winker, D. M.: On the nature and extent of optically thin marine low clouds, Journal of Geophysical Research: Atmospheres, 117, https://doi.org/https://doi.org/10.1029/2012JD017929, 2012.

Lohmann, U. and Feichter, J.: Impact of sulfate aerosols on albedo and lifetime of clouds: A sensitivity study with the ECHAM4 GCM, Journal of Geophysical Research: Atmospheres, 102, 13 685–13 700, https://doi.org/https://doi.org/10.1029/97JD00631, 1997.

Lohmann, U., Feichter, J., Chuang, C. C., and Penner, J. E.: Prediction of the number of cloud droplets in the ECHAM GCM, Journal of Geophysical Research: Atmospheres, 104, 9169–9198, https://doi.org/https://doi.org/10.1029/1999JD900046, 1999.

Lohmann, U., Stier, P., Hoose, C., Ferrachat, S., Kloster, S., Roeckner, E., and Zhang, J.: Cloud microphysics and aerosol indirect effects in the global climate model ECHAM5-HAM, Atmospheric Chemistry and Physics, 7, 3425–3446, https://doi.org/10.5194/acp-7-3425-2007, 2007.

Lundberg, S. M. and Lee, S. I.: A unified approach to interpreting model predictions, Advances in Neural Information Processing Systems, 2017-Decem, 4766–4775, 2017.

Lundberg, S. M., Erion, G. G., and Lee, S.-I.: Consistent Individualized Feature Attribution for Tree Ensembles, ArXiv, abs/1802.0, http://arxiv.org/abs/1802.03888, 2018.

Lundberg, S. M., Erion, G., Chen, H., DeGrave, A., Prutkin, J. M., Nair, B., Katz, R., Himmelfarb, J., Bansal, N., and Lee, S.-I.: From local explanations to global understanding with explainable AI for trees, Nature Machine Intelligence, 2, 56–67, https://doi.org/10.1038/s42256-019-0138-9, 2020.

Malavelle, F. F., Haywood, J. M., Jones, A., Gettelman, A., Clarisse, L., Bauduin, S., Allan, R. P., Karset, I. H. H., Kristjánsson, J. E., Oreopoulos, L., Cho, N., Lee, D., Bellouin, N., Boucher, O., Grosvenor, D. P., Carslaw, K. S., Dhomse, S., Mann, G. W., Schmidt, A., Coe, H., Hartley, M. E., Dalvi, M., Hill, A. A., Johnson, B. T., Johnson, C. E., Knight, J. R., O'Connor, F. M., Partridge, D. G., Stier, P., Myhre, G., Platnick, S., Stephens, G. L., Takahashi, H., and Thordarson, T.: Strong constraints on aerosol–cloud interactions from volcanic eruptions, Nature, 546, 485–491, https://doi.org/10.1038/nature22974, 2017.

Mauritsen, T., Bader, J., Becker, T., Behrens, J., Bittner, M., Brokopf, R., Brovkin, V., Claussen, M., Crueger, T., Esch, M., Fast, I., Fiedler, S., Fläschner, D., Gayler, V., Giorgetta, M., Goll, D. S., Haak, H., Hagemann, S., Hedemann, C., Hohenegger, C., Ilyina, T., Jahns, T., Jimenéz-de-la Cuesta, D., Jungclaus, J., Kleinen, T., Kloster, S., Kracher, D., Kinne, S., Kleberg, D., Lasslop, G., Kornblueh, L., Marotzke, J., Matei, D., Meraner, K., Mikolajewicz, U., Modali, K., Möbis, B., Müller, W. A., Nabel, J. E., Nam, C. C., Notz, D., Nyawira, S. S., Paulsen, H., Peters, K., Pincus, R., Pohlmann, H., Pongratz, J., Popp, M., Raddatz, T. J., Rast, S., Redler, R., Reick, C. H., Rohrschneider, T., Schemann, V., Schmidt, H., Schnur, R., Schulzweida, U., Six, K. D., Stein, L., Stemmler, I., Stevens, B., von Storch, J. S., Tian, F., Voigt, A., Vrese, P., Wieners, K. H., Wilkenskjeld, S., Winkler, A., and Roeckner, E.: Developments in the MPI-M Earth System Model version 1.2 (MPI-ESM1.2) and Its Response to Increasing CO2, Journal of Advances in Modeling Earth Systems, 11, 998–1038, https://doi.org/10.1029/2018MS001400, 2019.

Myers, T. A., Scott, R. C., Zelinka, M. D., Klein, S. A., Norris, J. R., and Caldwell, P. M.: Observational constraints on low cloud feedback reduce uncertainty of climate sensitivity, Nature Climate Change, 11, 501–507, https://doi.org/10.1038/s41558-021-01039-0, 2021.

Neubauer, D., Ferrachat, S., Siegenthaler-Le Drian, C., Stier, P., Partridge, D. G., Tegen, I., Bey, I., Stanelle, T., Kokkola, H., and Lohmann, U.: The global aerosol–climate model ECHAM6.3–HAM2.3 – Part 2: Cloud evaluation, aerosol radiative forcing, and climate sensitivity, Geoscientific Model Development, 12, 3609–3639, https://doi.org/10.5194/gmd-12-3609-2019, 2019.

Null, J.: El Niño and La Niña Years and Intensities Based on {Oceanic Niño Index (ONI)}, Golden Gate Weather Services, https://ggweather.com/enso/oni.htm, 2025.

Platnick, S. and Twomey, S.: Determining the Susceptibility of Cloud Albedo to Changes in Droplet Concentration with the Advanced Very High Resolution Radiometer, Journal of Applied Meteorology and Climatology, 33, 334–347, https://doi.org/https://doi.org/10.1175/1520-0450(1994)033<0334:DTSOCA>2.0.CO;2, 1994.

Quaas, J., Andrews, T., Bellouin, N., Block, K., Boucher, O., Ceppi, P., Dagan, G., Doktorowski, S., Eichholz, H. M., Forster, P., Goren, T., Gryspeerdt, E., Hodnebrog, Ø., Jia, H., Kramer, R., Lange, C., Maycock, A. C., Mülmenstädt, J., Myhre, G., O'Connor, F. M., Pincus, R., Samset, B. H., Senf, F., Shine, K. P., Smith, C., Stjern, C. W., Takemura, T., Toll, V., and Wall, C. J.: Adjustments to Climate Perturbations—Mechanisms, Implications, Observational Constraints, AGU Advances, 5, e2023AV001 144, https://doi.org/https://doi.org/10.1029/2023AV001144, 2024.

Roeckner, E., Arpe, K., Bengtsson, L., Christoph, M., Claussen, M., and Dümenil, L.: The atmospheric general circulation model ECHAM-4: Model description and simulation of present-day climate, Tech. Rep. 218, Max-Planck-Institut für Meteorologie, Hamburg, Germany, 1996.

Rosenfeld, D., Zhu, Y., Wang, M., Zheng, Y., Goren, T., and Yu, S.: Aerosol-driven droplet concentrations dominate coverage and water of oceanic low-level clouds, Science, 363, https://doi.org/10.1126/science.aav0566, 2019.

Rosenfeld, D., Kokhanovsky, A., Goren, T., Gryspeerdt, E., Hasekamp, O., Jia, H., Lopatin, A., Quaas, J., Pan, Z., and Sourdeval, O.: Frontiers in Satellite-Based Estimates of Cloud-Mediated Aerosol Forcing, Reviews of Geophysics, 61, e2022RG000 799, https://doi.org/https://doi.org/10.1029/2022RG000799, 2023.

Salzmann, M., Ferrachat, S., Tully, C., Münch, S., Watson-Parris, D., Neubauer, D., Siegenthaler-Le Drian, C., Rast, S., Heinold, B., Crueger, T., Brokopf, R., Mülmenstädt, J., Quaas, J., Wan, H., Zhang, K., Lohmann, U., Stier, P., and Tegen, I.: The Global Atmosphere-aerosol Model ICON-A-HAM2.3–Initial Model Evaluation and Effects of Radiation Balance Tuning on Aerosol Optical Thickness, Journal of Advances in Modeling Earth Systems, 14, e2021MS002 699, https://doi.org/https://doi.org/10.1029/2021MS002699, 2022.

Sherwood, S. C., Bony, S., Boucher, O., Bretherton, C., Forster, P. M., Gregory, J. M., and Stevens, B.: Adjustments in the forcing-feedback framework for understanding climate change, Bulletin of the American Meteorological Society, 96, 217–228, https://doi.org/10.1175/BAMS-D-13-00167.1, 2015.

Small, J. D., Chuang, P. Y., Feingold, G., and Jiang, H.: Can aerosol decrease cloud lifetime?, Geophysical Research Letters, 36, 1–5, https://doi.org/10.1029/2009GL038888, 2009.

Smith, C. J., Kramer, R. J., Myhre, G., Alterskjær, K., Collins, W., Sima, A., Boucher, O., Dufresne, J.-L., Nabat, P., Michou, M., Yukimoto, S., Cole, J., Paynter, D., Shiogama, H., O'Connor, F. M., Robertson, E., Wiltshire, A., Andrews, T., Hannay, C., Miller, R., Nazarenko, L., Kirkevåg, A., Olivié, D., Fiedler, S., Lewinschal, A., Mackallah, C., Dix, M., Pincus, R., and Forster, P. M.: Effective radiative forcing and adjustments in CMIP6 models, Atmospheric Chemistry and Physics, 20, 9591–9618, https://doi.org/10.5194/acp-20-9591-2020, 2020.

Sundqvist, H., Berge, E., and Kristjánsson, J. E.: Condensation and Cloud Parameterization Studies with a Mesoscale Numerical Weather Prediction Model, Monthly Weather Review, 117, 1641–1657, https://doi.org/https://doi.org/10.1175/1520-0493(1989)117<1641:CACPSW>2.0.CO;2, 1989.

Taylor, K. E., Williamson, D., and Zwiers, F.: PCMDI Report - Number 60 - The sea surface temperature and sea-ice concentration boundary conditions for AMIP II simulations, https://doi.org/10.5281/zenodo.13835219, 2000.

Toll, V., Christensen, M., Quaas, J., and Bellouin, N.: Weak average liquid-cloud-water response to anthropogenic aerosols, Nature, 572, 51–55, https://doi.org/10.1038/s41586-019-1423-9, 2019.

Twomey, S.: The Influence of Pollution on the Shortwave Albedo of Clouds, Journal of the Atmospheric Sciences, 34, 1149–1152, https://doi.org/10.1175/1520-0469(1977)034<1149:tiopot>2.0.co;2, 1977.

Wall, C. J., Norris, J. R., Possner, A., McCoy, D. T., McCoy, I. L., and Lutsko, N. J.: Assessing effective radiative forcing from aerosol–cloud interactions over the global ocean, Proceedings of the National Academy of Sciences, 119, e2210481 119, https://doi.org/10.1073/pnas.2210481119, 2022.

Wall, C. J., Storelvmo, T., and Possner, A.: Global observations of aerosol indirect effects from marine liquid clouds, Atmospheric Chemistry and Physics, 23, 13 125–13 141, https://doi.org/10.5194/acp-23-13125-2023, 2023.

Wang, M. and Penner, J. E.: Aerosol indirect forcing in a global model with particle nucleation, Atmospheric Chemistry and Physics, 9, 239–260, https://doi.org/10.5194/acp-9-239-2009, 2009.

Wang, S., Wang, Q., and Feingold, G.: Turbulence, Condensation, and Liquid Water Transport in Numerically Simulated Nonprecipitating Stratocumulus Clouds, Journal of the Atmospheric Sciences, 60, 262–278, https://doi.org/https://doi.org/10.1175/1520-0469(2003)060<0262:TCALWT>2.0.CO;2, 2003.

Wang, X., Mao, F., Zhu, Y., Rosenfeld, D., Pan, Z., Zang, L., Lu, X., Liu, F., and Gong, W.: Hidden Large Aerosol-Driven Cloud Cover Effect Over High-Latitude Ocean, Journal of Geophysical Research: Atmospheres, 129, e2023JD039 312, https://doi.org/https://doi.org/10.1029/2023JD039312, 2024.

Wang, Y., Neubauer, D., Chen, Y., Jordan, G., Malavelle, F., Yuan, T., Partridge, D., Field, P., Wang, H., Wang, M., Michou, M., Nabat, P., Laakso, A., Myhre, G., and Lohmann, U.: Challenges in global climate models to represent cloud response to aerosols: insights from volcanic eruptions, Nature Communications, 17, 627, https://doi.org/10.1038/s41467-025-67359-3, 2025.

Watson-Parris, D. and Smith, C. J.: Large uncertainty in future warming due to aerosol forcing, Nature Climate Change, 12, 1111–1113, https://doi.org/10.1038/s41558-022-01516-0, 2022.

Wood, R.: Stratocumulus Clouds, Monthly Weather Review, 140, 2373–2423, https://doi.org/10.1175/MWR-D-11-00121.1, 2012.

Wood, R., Wyant, M., Bretherton, C. S., Rémillard, J., Kollias, P., Fletcher, J., Stemmler, J., de Szoeke, S., Yuter, S., Miller, M., Mechem, D., Tselioudis, G., Chiu, J. C., Mann, J. A. L., O'Connor, E. J., Hogan, R. J., Dong, X., Miller, M., Ghate, V., Jefferson, A., Min, Q., Minnis, P., Palikonda, R., Albrecht, B., Luke, E., Hannay, C., and Lin, Y.: Clouds, Aerosols, and Precipitation in the Marine Boundary Layer: An Arm Mobile Facility Deployment, Bulletin of the American Meteorological Society, 96, 419–440, https://doi.org/10.1175/BAMS-D-13-00180.1, 2015.

Xu, K.-M. and Randall, D. A.: A Semiempirical Cloudiness Parameterization for Use in Climate Models, Journal of Atmospheric Sciences, 53, 3084–3102, https://doi.org/https://doi.org/10.1175/1520-0469(1996)053<3084:ASCPFU>2.0.CO;2, 1996.

Yuan, T., Song, H., Wood, R., Oreopoulos, L., Platnick, S., Wang, C., Yu, H., Meyer, K., and Wilcox, E.: Observational evidence of strong forcing from aerosol effect on low cloud coverage, https://doi.org/10.1126/sciadv.adh7716, 2023.

Zelinka, M. D., Andrews, T., Forster, P. M., and Taylor, K. E.: Quantifying components of aerosol-cloud-radiation interactions in climate models, Journal of Geophysical Research: Atmospheres, 119, 7599–7615, https://doi.org/10.1002/2014JD021710, 2014.

Zelinka, M. D., Smith, C. J., Qin, Y., and Taylor, K. E.: Comparison of methods to estimate aerosol effective radiative forcings in climate models, Atmospheric Chemistry and Physics, 23, 8879–8898, https://doi.org/10.5194/acp-23-8879-2023, 2023.